

Title: Turbulence and mixing from neighbouring stratified shear layers

Authors:

Chih-Lun Liu<sup>1</sup>, Alexis K. Kaminski<sup>2</sup>, William D. Smyth<sup>1</sup>

<sup>1</sup>College of Earth, Ocean and Atmospheric Sciences, Oregon State University,  
Corvallis, OR 97331

<sup>2</sup>Department of Mechanical Engineering, University of California, Berkeley, Berkeley,  
CA, 94720

This preprint was submitted to the Journal of Fluid Mechanics for peer review, so the manuscript is not yet peer reviewed.

Banner appropriate to article type will appear here in typeset article

# Turbulence and mixing from neighbouring stratified shear layers

Chih-Lun Liu<sup>1</sup>†, Alexis K. Kaminski<sup>2</sup>, William D. Smyth<sup>1</sup>,

<sup>1</sup>College of Earth, Ocean and Atmospheric Sciences, Oregon State University, Corvallis, OR 97331.

<sup>2</sup>Department of Mechanical Engineering, University of California, Berkeley, Berkeley, CA, 94720.

(Received xx; revised xx; accepted xx)

10 March 2024

Studies of Kelvin-Helmholtz instability (KHI) have typically modeled the initial mean flow as an isolated stratified shear layer. However, geophysical flows frequently exhibit multiple layers. As a step towards understanding these flows, we examine the case of two adjacent stratified shear layers using both linear stability analysis and direct numerical simulation. With sufficiently large layer separation, the characteristics of instability and mixing converge toward the familiar Kelvin-Helmholtz turbulence. Similarly, when the separation is near zero and the layers add to make a single layer, albeit with a reduced Richardson number. Here, our focus is on intermediate separations, which produce new and complex phenomena. As the separation distance  $D$  increases from zero to a critical value  $D_c$ , approximately half the thickness of the shear layer, the growth rate and wavenumber both decrease monotonically. The minimum Richardson number is relatively low, potentially inducing pairing, and shear-aligned convective instability (SCI) is the primary mechanism for transition. Consequently, mixing is relatively strong and efficient. When  $D \sim D_c$ , billow length is increased but growth is slowed. Despite the modest growth rate, mixing is strong and efficient, engendered primarily by secondary shear instability (SSI) manifested on the braids, and by SCI occurring on the eyelids. Shear-aligned vortices are driven in part by buoyancy production; however, shear production and vortex stretching are equally important mechanisms. When  $D > D_c$ , neighbouring billow interactions suppress the growth of both KHI and SCI. Strength and efficiency of mixing decrease abruptly as  $D_c$  is exceeded. As turbulence decays, layers of marginal instability may arise.

## 1. Introduction

The accuracy of large-scale climate and ocean models depends on the parameterization of turbulent fluxes. Turbulent mixing events are often modeled using idealized shear instabilities in stratified flows. Shear instability has been observed in the stably stratified nocturnal atmospheric boundary layer (Newsom & Banta 2003; Smyth *et al.* 2023) as well as at higher elevations (Fritts *et al.* 2023). Shear instability has also been observed in a variety of oceanic contexts, including equatorial undercurrents (Moum *et al.* 2011), flows over sills (Van Haren *et al.* 2014; Chang *et al.* 2022), estuarine shear zones (Geyer *et al.* 2010; Holleman *et al.*

† Email address for correspondence: [chihlunl@gmail.com](mailto:chihlunl@gmail.com)

35 2016; Tu *et al.* 2022) and the strongly-stratified transition layer within the ocean surface  
36 boundary layer (Kaminski *et al.* 2021).

37 Previous theoretical research on shear instabilities has assumed a single, isolated stratified  
38 shear layer (e.g. Caulfield & Peltier 2000; Mashayek & Peltier 2013; Salehipour & Peltier  
39 2015; Kaminski & Smyth 2019; Lewin & Caulfield 2021; Liu *et al.* 2022, 2023), neglecting  
40 the potential influence of nearby flow structures. Our goal here is to relax the assumption of  
41 a single, isolated shear layer. As a starting point, we examine a pair of shear layers, varying  
42 the distance between them and analyzing the resulting changes in the route to turbulence and  
43 in the resulting mixing.

44 This is the third in a sequence of three studies using ensembles of direct numerical  
45 simulations (DNS) with small, random variations in the initial state. Liu *et al.* (2022, hereafter  
46 L22) showed that even a slight change in the initial perturbation can lead to significant  
47 variations in turbulence timing and strength due to interactions between the primary KH,  
48 subharmonic, and 3-D secondary instabilities. This resulted in differences of up to a factor of  
49 four in the maximum turbulent kinetic energy and a factor of two in the potential energy gain  
50 due to mixing. Liu *et al.* (2023, hereafter L23) studied the effects of boundary proximity on  
51 KH instability. Boundary effects have a pronounced effect on the dynamics of KH instability,  
52 influencing its growth, secondary instability, and the resulting turbulent mixing. Notably, the  
53 cumulative mixing efficiency vanishes as the shear layer approaches a solid boundary. As in  
54 L22, these results were sensitive to small changes in the initial conditions, emphasizing the  
55 need to compare ensemble-averaged statistics.

56 Our work is motivated in part by observations of multiple stratified shear layers in  
57 geophysical fluids at consecutive depths, sometimes in close proximity to each other  
58 (Desaubies & Smith 1982; Alford & Pinkel 2000). Fritts *et al.* (2003) showed layered  
59 structures in the atmosphere due to shear instability and gravity-wave breaking. Recent work  
60 on stratified shear flows reveals spontaneous organization into layers of quiescent, strongly  
61 stratified fluid and strongly turbulent, weakly stratified fluid (Woods 1968; Caulfield 2021).  
62 We therefore wonder about conditions under which instabilities of nearby shear layers could  
63 interact, and with what effect on instability, turbulence and mixing.

64 We find that, as the separation distance between the two layers decreases to (approximately)  
65 the layer thickness, instability is suppressed. We also show that the presence of a neighbouring  
66 shear layer can excite one of two novel forms of instability, one stationary and one oscillatory.  
67 This distinction has profound effects on the transition to turbulence and the resulting mixing,  
68 including an abrupt change in mixing efficiency, even when the difference in initial states is  
69 small.

70 In §2 we describe the setup for our numerical simulations and the choice of the initial  
71 parameter values as well as the diagnostic tools required for the analysis of three-dimensional  
72 energetics and mixing. We then describe the effects of neighbouring shear instability on the  
73 linear stability characteristics in §3, and introduce the stationary and oscillatory modes  
74 of instability. In §4, we analyze the perturbation kinetic energy budget to explain how  
75 a neighbouring shear instability could alter the route to turbulence. In §5, we describe  
76 the neighbouring effects on the irreversible mixing and mixing efficiency. Conclusions are  
77 summarized in section §6, and possible directions for future research are discussed in §7.

## 78 2. Methodology

79

### 2.1. The mathematical model

80 We begin by considering a stably-stratified parallel shear flow,

81
$$U^*(z) = U_0^* \left[ \tanh\left(\frac{z^* - D^*}{h^*}\right) + \tanh\left(\frac{z^* + D^*}{h^*}\right) \right] \quad \text{and} \quad (2.1)$$

82
$$B^*(z) = B_0^* \left[ \tanh\left(\frac{z^* - D^*}{h^*}\right) + \tanh\left(\frac{z^* + D^*}{h^*}\right) \right] \quad (2.2)$$

83 in which  $2U_0^*$  and  $2B_0^*$  are, respectively, velocity and buoyancy differences across the  
 84 individual shear layer and  $2h^*$  is its thickness (figure 1). Both stratified shear layers have a  
 85 distance  $D^*$  from the center of the domain (so that the distance between the centers is  $2D^*$ ).  
 86 The domain has a vertical extent  $L_z^*$  with upper and lower boundaries at  $\pm L_z^*/2$ . Asterisks  
 87 indicate dimensional quantities. The Cartesian coordinates are  $x^*$  (streamwise),  $y^*$  (spanwise)  
 88 and  $z^*$  (vertical, positive upwards), and the corresponding velocity components are  $u^*$ ,  $v^*$  and  
 89  $w^*$ . After nondimensionalizing velocities by  $U_0^*$ , buoyancy by  $B_0^*$ , lengths by  $h^*$  and times by  
 90 the advective timescale  $h^*/U_0^*$ , (2.1) and (2.2) become:

91
$$U(z) = B(z) = \tanh(z - D) + \tanh(z + D). \quad (2.3)$$

92 The evolution of the flow is governed by the Boussinesq Navier-Stokes equations, as well  
 93 as the equations of buoyancy conservation and mass continuity. Nondimensionalized, these  
 94 are:

95
$$\frac{\partial \mathbf{u}}{\partial t} + \mathbf{u} \cdot \nabla \mathbf{u} = -\nabla p + Ri_0 b \hat{z} + \frac{1}{Re_0} \nabla^2 \mathbf{u}, \quad (2.4)$$

96
$$\frac{\partial b}{\partial t} + \mathbf{u} \cdot \nabla b = \frac{1}{Re_0 Pr} \nabla^2 b, \quad (2.5)$$

97
$$\nabla \cdot \mathbf{u} = 0, \quad (2.6)$$

98 where  $p$  is the pressure and  $\hat{z}$  is the vertical unit vector. The equations involve three  
 99 dimensionless parameters: the initial Reynolds number,  $Re_0 = U_0^* h^*/\nu^*$ , where  $\nu^*$  is the  
 100 kinematic viscosity; the Prandtl number,  $Pr = \nu^*/\kappa^*$ , where  $\kappa^*$  is the diffusivity; and the  
 101 initial bulk Richardson number,  $Ri_0 = B_0^* h^*/U_0^{*2}$ .

102 In general, we define the gradient Richardson number as:

103
$$Ri_g(z, t) = \frac{\partial \langle b^* \rangle_{xy} / \partial z^*}{(\partial \langle u^* \rangle_{xy} / \partial z^*)^2} = Ri_0 \frac{\partial \langle b \rangle_{xy} / \partial z}{(\partial \langle u \rangle_{xy} / \partial z)^2} = \frac{N^2}{S^2}. \quad (2.7)$$

104 Here, the notation  $\langle \rangle_r$  represents an average over  $r$ , where  $r$  can encompass any combination  
 105 of  $x$ ,  $y$ ,  $z$  and  $t$ .  $N^2$  is the squared buoyancy frequency and  $S$  is the mean shear. The minimum  
 106 of  $Ri_g$  with respect to  $z$  is denoted as  $Ri_{min}(t)$ . In the inviscid limit, a necessary condition for  
 107 instability is that  $Ri_{min}$  be less than  $1/4$  (Miles 1961; Howard 1961). For the flow described  
 108 by (2.3), the initial  $Ri_{min}$  increases from  $Ri_0/2$  to  $Ri_0$  when  $D$  increases from 0 to infinity  
 109 (figure 2).

110 Boundary conditions are periodic in both horizontal directions with periodicity intervals  
 111  $L_x$  and  $L_y$ . The upper and lower boundaries are free-slip ( $\partial u / \partial z = \partial v / \partial z = 0$ ), insulating  
 112 ( $\partial b / \partial z = 0$ ) and impermeable ( $w = 0$ ).

113 A small, random velocity perturbation is incorporated into the initial state (2.3). This initial  
 114 perturbation field is purely stochastic and is applied uniformly to all three velocity components  
 115 across the computational domain. The maximum amplitude of any single component is

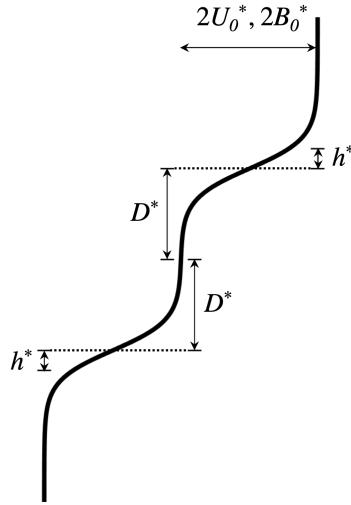


Figure 1: Initial mean profile for velocity and buoyancy showing dimensional parameters as defined in (2.1) and (2.2).

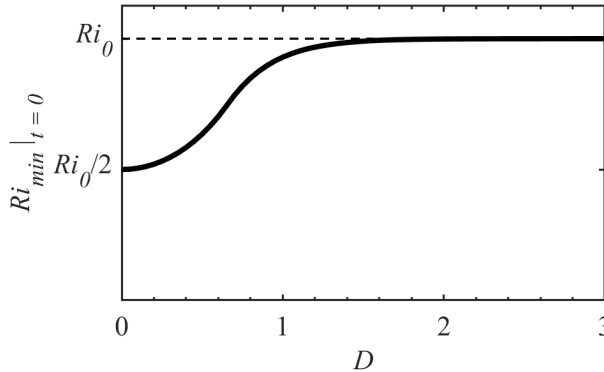


Figure 2: The dependence of initial minimum Richardson number  $Ri_{min}$  on  $D$ .  $Ri_0$  is 0.16 in the present case.

116 limited to 0.05, equivalent to 2.5% of the velocity change across each shear layer. This  
 117 magnitude is kept small to ensure that the initial growth phase is consistent with linear  
 118 perturbation theory. For each value of  $D$ , an ensemble of three cases is simulated, each using  
 119 a distinct seed to generate the random velocities (L22).

120

## 2.2. Linear Stability Analysis

121 To evaluate the linear instabilities, (2.4-2.6) are linearized about the initial base flow (2.3).  
 122 These equations are then subjected to perturbations induced by small amplitude, normal  
 123 mode disturbances proportional to the real part of  $a(z) \exp(\sigma t + ikx)$ . In this context,  $a(z)$   
 124 denotes the vertically-varying, complex amplitude of any perturbation quantity,  $\sigma$  stands for  
 125 the complex exponential growth rate, and  $k$  is the wavenumber in the streamwise direction.  
 126 The streamwise phase speed is  $c = i\sigma/k$ . The normal mode equations are discretized using

---

$D$	$(L_x, L_y, L_z)$	$(N_x, N_y, N_z)$	$Ri_{min}$
0	(28.56, 7.14, 30)	(576, 144, 613)	0.08
0.5	(36.96, 9.24, 30)	(768, 192, 613)	0.10
1	(78.54, 19.64, 30)	(1536, 384, 613)	0.15
2	(29.92, 7.48, 30)	(576, 144, 613)	0.16
3	(28.56, 7.14, 30)	(576, 144, 613)	0.16
$\infty$	(27.76, 6.94, 20)	(512, 128, 361)	0.16

---

Table 1: Parameter values for five, 3-member DNS ensembles. In all cases  $Re_0 = 1000$ ,  $Pr = 1$ ,  $Ri_0 = 0.16$ . Data for the case  $D = \infty$  is sourced from L22 and includes only a single, isolated shear layer. The maximum initial random velocity component is 0.05.

---

127 a Fourier-Galerkin method, yielding a generalized matrix eigenvalue problem that is solved  
 128 using standard methods. Details may be found in SC19’s §13.3 or in Lian *et al.* (2020).

129

### 2.3. Direct Numerical Simulations

130 Simulations are conducted using DIABLO (Taylor 2008), which utilizes a hybrid implicit-  
 131 explicit time-stepping scheme with pressure projection. The viscous and diffusive com-  
 132 ponents are addressed implicitly using second-order Crank-Nicolson method, while other  
 133 terms are explicitly resolved employing a third-order Runge-Kutta-Wray method. The  
 134 vertical  $z$  direction dependence is discretized using second-order finite-differences, whereas  
 135 the periodic streamwise and spanwise directions ( $x$ ,  $y$ ) are managed using the Fourier  
 136 pseudospectral method.

137 To allow subharmonic mode growth, we set the streamwise periodicity interval,  $L_x$ , to two  
 138 wavelengths of the fastest-growing KH mode, as determined through linear stability analysis  
 139 (section 2.2). For the development of 3-D secondary instabilities, a spanwise periodicity  
 140 interval of  $L_y = L_x/4$  is adequate (e.g. Klaassen & Peltier 1985; Mashayek & Peltier  
 141 2013). The domain height is  $L_z = 30$  to minimize boundary effects. The computational  
 142 grid is uniform and isotropic and resolves  $\sim 2.5$  times the Kolmogorov length scale,  $L_k =$   
 143  $(Re^{-3}/\epsilon)^{1/4}$ , with  $\epsilon$  representing a characteristic viscous dissipation rate after turbulence  
 144 onset (e.g. Smyth & Moum 2000). Grid sizes are given in table 1.

145 Given the sensitivity of turbulent flows to initial conditions, we work with ensemble mean  
 146 statistics where appropriate. Following L22, we use an ensemble of three cases at each  
 147 separation distance  $D$ . Five values of  $D$  are considered, for a total of 15 simulations (listed  
 148 in table 1). We also employ a 3-member ensemble of simulations of a single shear layer  
 149 described in L22 to represent the limiting case  $D \rightarrow \infty$ .

150 To maintain our primary focus on the influence of the adjacent shear layer, we keep the  
 151 initial state parameters, specifically the Richardson, Reynolds, and Prandtl numbers, fixed.  
 152 The choice  $Ri_0 = 0.16$  is large enough for the pairing instability (e.g. Klaassen & Peltier  
 153 1989) to be damped by stratification when  $Ri_{min} = Ri_0$  (i.e. for large  $D$ ). In all cases, we set  
 154  $Re_0 = 1000$  and  $Pr = 1$ . While smaller than would be typical in nature, these values reflect  
 155 a necessary compromise dictated by computational resource constraints.

156

### 2.4. Diagnostics

157 The total velocity field can be decomposed into a horizontally-averaged component, referred  
 158 to as the mean flow, and a perturbation:

159 
$$\mathbf{u}(x, y, z, t) = \overline{U}\hat{\mathbf{e}}^{(x)} + \mathbf{u}'(x, y, z, t), \quad \text{where } \overline{U}(z, t) = \langle u \rangle_{xy}, \quad (2.8)$$

160 where  $\hat{\mathbf{e}}^{(x)}$  is the unit vector in the streamwise direction. Following Caulfield & Peltier  
 161 (2000), the perturbation velocity is further subdivided into two-dimensional (2-D) and three-  
 162 dimensional (3-D) components

163 
$$\mathbf{u}'(x, y, z, t) = \mathbf{u}_{2d} + \mathbf{u}_{3d}, \quad (2.9)$$

164 where

165 
$$\mathbf{u}_{2d}(x, z, t) = \langle \mathbf{u} \rangle_y - \overline{U}\hat{\mathbf{e}}^{(x)} \quad \text{and} \quad \mathbf{u}_{3d}(x, y, z, t) = \mathbf{u} - \mathbf{u}_{2d} - \overline{U}\hat{\mathbf{e}}^{(x)} = \mathbf{u} - \langle \mathbf{u} \rangle_y. \quad (2.10)$$

166 Similarly, the buoyancy field can be decomposed as:

167 
$$b(x, y, z, t) = \overline{B} + b'(x, y, z, t), \quad \text{where } \overline{B}(z, t) = \langle b \rangle_{xy}, \quad (2.11)$$

168 
$$b_{3d}(x, y, z, t) = b - \langle b \rangle_y. \quad (2.12)$$

169 The total kinetic energy can now be partitioned as

170 
$$\mathcal{K} = \overline{\mathcal{K}} + \mathcal{K}'; \quad \mathcal{K}' = \mathcal{K}_{2d} + \mathcal{K}_{3d}, \quad (2.13)$$

171 where

172 
$$\overline{\mathcal{K}} = \frac{1}{2} \langle \overline{U}^2 \rangle_z, \quad \mathcal{K}_{2d} = \frac{1}{2} \langle u_{2d}^2 + v_{2d}^2 + w_{2d}^2 \rangle_{xz}, \quad \mathcal{K}_{3d} = \frac{1}{2} \langle u_{3d}^2 + v_{3d}^2 + w_{3d}^2 \rangle_{xyz}. \quad (2.14)$$

173 These constituent kinetic energies  $\overline{\mathcal{K}}$ ,  $\mathcal{K}'$ ,  $\mathcal{K}_{2d}$  and  $\mathcal{K}_{3d}$  can be identified as the horizontally-  
 174 averaged kinetic energy associated with the mean flow, the turbulent kinetic energy, and the  
 175 kinetic energy related to 2-D and 3-D motions. We denote the instances in time when  $\mathcal{K}_{2d}$   
 176 and  $\mathcal{K}_{3d}$  reach their maximum values as  $t_{2d}$  and  $t_{3d}$ , respectively.

177 Quantification of irreversible mixing involves decomposing the total potential energy  $\mathcal{P} =$   
 178  $-Ri_0 \langle bz \rangle_{xyz}$  into available and background components,  $\mathcal{P} = \mathcal{P}_a + \mathcal{P}_b$ . The background  
 179 potential energy,  $\mathcal{P}_b$ , is the minimum potential energy achievable by adiabatically rearranging  
 180 the buoyancy field into a statically stable state  $b^*$  (Winters *et al.* 1995; Tseng & Ferziger  
 181 2001). After computing the total and background potential energy, the available potential  
 182 energy is determined from the residual,  $\mathcal{P}_a = \mathcal{P} - \mathcal{P}_b$ .  $\mathcal{P}_a$  represents the potential energy  
 183 available for conversion to kinetic energy, arising from lateral variations in buoyancy or  
 184 statically unstable regions.

185 The irreversible mixing rate due to fluid motions is defined as,

186 
$$\mathcal{M} = \frac{d\mathcal{P}_b}{dt} - \mathcal{D}_p, \quad (2.15)$$

187 where

188 
$$\mathcal{D}_p = \frac{Ri_0(b_{top} - b_{bottom})}{Re_0 Pr L_z} \quad (2.16)$$

189 refers to the rate at which the potential energy of a statically stable buoyancy distribution  
 190 would increase solely due to diffusion of the mean buoyancy profile in the absence of any  
 191 fluid motion.

192 There exists a variety of definitions for mixing efficiency in the literature (e.g. Gregg *et al.*  
 193 2018). Here, we define the instantaneous mixing efficiency as

194 
$$\eta_i = \frac{\mathcal{M}}{\mathcal{M} + \epsilon}, \quad (2.17)$$

195 where  $\epsilon = \frac{2}{Re} \langle s_{ij}s_{ij} \rangle_{xyz}$  is the total dissipation rate, and  $s_{ij} = (\partial u_i/\partial x_j + \partial u_j/\partial x_i)/2$   
 196 is the strain rate tensor. The mixing efficiency quantifies the fraction of energy directed  
 197 towards irreversible mixing to the total kinetic energy loss that is irreversibly lost to friction  
 198 (Peltier & Caulfield 2003). The cumulative mixing efficiency serves as a valuable measure  
 199 for quantifying the overall efficiency of the entire mixing process, and is defined as

$$200 \quad \eta_c = \frac{\int_{t_i}^{t_f} \mathcal{M} dt}{\int_{t_i}^{t_f} \mathcal{M} dt + \int_{t_i}^{t_f} \epsilon dt}, \quad (2.18)$$

201 where  $t_i \sim 2$ , is the initial time after the model adjustment period, and  $t_f$  is the final time of  
 202 the integral at which  $\mathcal{M} = \mathcal{D}_p$ .

203 An alternative quantifier of mixing that readily shows the spatial structure is the perturba-  
 204 tion buoyancy variance dissipation rate, defined as

$$205 \quad \chi'(x, y, z, t) = \frac{2Ri_0}{RePr} |\nabla b'|^2, \quad (2.19)$$

206 where  $b'$  is the buoyancy perturbation, representing the deviation from the horizontal mean  
 207 buoyancy.

208 The evolution equation for the kinetic energy of 3-D perturbations can be expressed in the  
 209 form (Caulfield & Peltier 2000)

$$210 \quad \sigma_{3d} = \frac{1}{2\mathcal{K}_{3d}} \frac{d}{dt} \mathcal{K}_{3d} \quad (2.20)$$

$$211 \quad = \mathcal{R}_{3d} + \mathcal{S}h_{3d} + \mathcal{A}_{3d} + \mathcal{H}_{3d} + \mathcal{D}_{3d}, \quad (2.21)$$

212 where the first two terms represent the 3-D perturbation kinetic energy extraction from the  
 213 background mean shear and the background 2-D KH billow by means of Reynolds stresses,  
 214 respectively defined as

$$215 \quad \mathcal{R}_{3d} = -\frac{1}{2\mathcal{K}_{3d}} \left\langle u_{3d} w_{3d} \frac{\partial \bar{U}}{\partial z} \right\rangle_{xyz}, \quad (2.22)$$

$$216 \quad \mathcal{S}h_{3d} = -\frac{1}{2\mathcal{K}_{3d}} \left\langle u_{3d} w_{3d} \left( \frac{\partial u_{2d}}{\partial z} + \frac{\partial w_{2d}}{\partial x} \right) \right\rangle_{xyz}. \quad (2.23)$$

217 The third term represents the stretching deformation of the 3-D motions and is defined as

$$218 \quad \mathcal{A}_{3d} = -\frac{1}{2\mathcal{K}_{3d}} \left\langle \frac{1}{2} \left( u_{3d}^2 - w_{3d}^2 \right) \left( \frac{\partial u_{2d}}{\partial x} - \frac{\partial w_{2d}}{\partial z} \right) \right\rangle_{xyz}. \quad (2.24)$$

219 The final two terms are the buoyancy production term and the negative-definite viscous  
 220 dissipation term associated with 3-D perturbations and are defined respectively as

$$221 \quad \mathcal{H}_{3d} = \frac{Ri_0}{2\mathcal{K}_{3d}} \langle b_{3d} w_{3d} \rangle_{xyz}, \quad (2.25)$$

$$222 \quad \mathcal{D}_{3d} = -\frac{1}{\mathcal{K}_{3d} Re} \langle s_{ij}s_{ij} \rangle_{xyz}, \quad (2.26)$$

223 where  $s_{ij}$  is the strain rate tensor of the 3-D motions. The time at which  $\sigma_{3d}$  is a maximum  
 224 is defined as  $t_{\sigma_{3d}}$ . The enstrophy in the three vorticity components is defined as

$$225 \quad \mathcal{Z}_x = \frac{1}{2} (\omega_x^2), \quad \mathcal{Z}_y = \frac{1}{2} (\omega_y^2), \quad \mathcal{Z}_z = \frac{1}{2} (\omega_z^2) \quad (2.27)$$



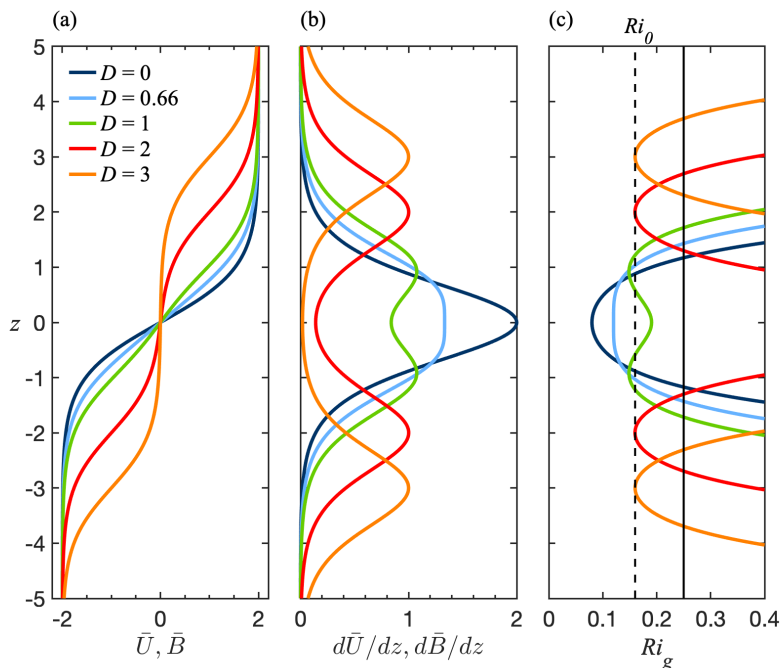


Figure 3: Profiles of (a) horizontally averaged velocity and buoyancy (b) mean velocity and mean buoyancy gradient and (c) gradient Richardson number. Vertical dashed line in (c) shows  $Ri_0$  and the vertical solid line denotes the stability criterion  $1/4$ .

226 where  $\omega_x = \frac{\partial w}{\partial y} - \frac{\partial v}{\partial z}$ ,  $\omega_y = \frac{\partial u}{\partial z} - \frac{\partial w}{\partial x}$ , and  $\omega_z = \frac{\partial v}{\partial x} - \frac{\partial u}{\partial y}$ .

### 227 3. The Primary Linear Instability

228 In the extreme cases,  $D = 0$  and  $D \rightarrow \infty$ , (2.3) is equivalent to one or two isolated shear  
 229 layers which produce standard KH instabilities (e.g. Hazel 1972; Smyth & Carpenter 2019)  
 230 if  $Ri_0 < 1/4$ . In the previously unexplored cases with finite, nonzero  $D$ , (2.3) represents a  
 231 superposition of two shear layers whose modes of instability interact in complex ways.

232 In the case  $D = 0$ , (2.3) becomes  $U(z) = B(z) = 2 \tanh(z)$ , i.e. the two shear layers  
 233 sum to make a single stratified shear layer with doubled shear and stratification (dark blue  
 234 curve in figure 3). The corresponding  $Ri_{min}$  is  $Ri_0/2 = 0.08$ . The dominant mode is the  
 235 stationary Kelvin-Helmholtz mode with a fastest-growing wavenumber of 0.44. We term this  
 236 a stationary mode because there is only a single fastest-growing mode for a given initial  
 237 state. (This is in contrast to oscillatory instability, discussed below, which is a superposition  
 238 of two modes with equal growth rates but different phase speeds.) In the reference frame  
 239 assumed here, the phase speed of the stationary mode is zero, while the two phase speeds of  
 240 the oscillatory mode are opposites.

241 As  $D$  increases to  $\tanh^{-1} \sqrt{1/3}$  (approximately 0.66), the single shear maximum at  $z = 0$   
 242 widens (light blue curve in figure 3b). Therefore the wavenumber of the fastest-growing  
 243 mode decreases, the growth rate decreases (figure 4, red curve), and  $Ri_{min}$  increases (figure  
 244 3c, light blue curve). The corresponding mode is a continuation of the stationary mode found  
 245 at  $D = 0$  as discussed above. It may be thought of as a KH-like instability of the two shear  
 246 layers *in toto*, rather than of one or the other layer.

247 If  $D$  slightly exceeds  $\tanh^{-1} \sqrt{1/3}$ , two small shear maxima appear slightly above and

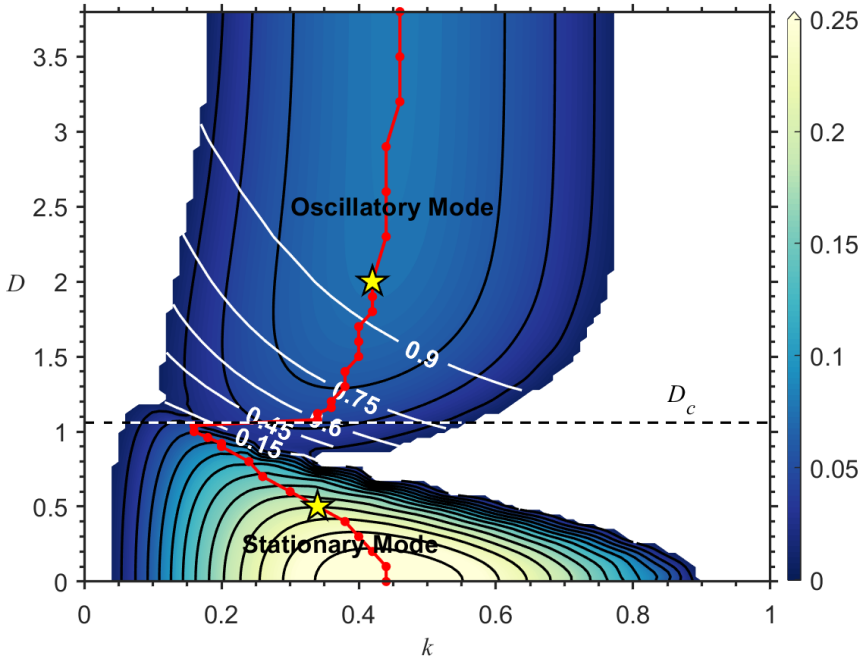


Figure 4: Stability diagram showing the transition from stationary mode to the oscillatory mode as  $D$  increases, with  $Re = 1000$ ,  $Pr = 1$ ,  $Ri_0 = 0.16$ , and boundaries at  $z = \pm L_z/2 = \pm 15$ . Colours and black contours represent the growth rate of the fastest-growing mode on the  $k - D$  plane. The contour interval is 0.02. White contours show the (positive) phase velocity. Horizontal dashed line denotes the critical distance  $D_c$  (1.06). Stars highlight the cases  $D = 0.5$  and  $D = 2$ , where the eigenfunctions of the fastest-growing modes are shown in figure 7.

248 below  $z = 0$ . These produce two inflectional instabilities having equal (though small) growth  
 249 rates and equal but opposite phase velocities. (Only the positive phase velocity is shown on  
 250 figure 4.) Combined, these modes result in an oscillatory instability. As  $D$  increases further,  
 251 the oscillatory and stationary modes coexist (figure 4). The shear maxima become weaker but  
 252 more distinct (green curve in figure 3b). The growth rate of the oscillatory mode increases  
 253 while that of the stationary mode continues to decrease (figure 4). The two modes attain  
 254 equal growth rates at a critical separation distance  $D = D_c$ , with  $D_c = 1.06$  in the present  
 255 case  $Ri_{min} = 0.16$  (dashed horizontal lines in figure 4 and 5). More generally,  $D_c$  decreases  
 256 slightly with increasing  $Ri_0$  (figure 5).

257 At higher  $D$  (about 1.2 in our case) the stationary mode is stabilized while the growth rate  
 258 of the oscillatory mode continues to increase with increasing  $D$  (figure 4). When  $D = 3$ , for  
 259 example, the two shear maxima are separated by a weakly stratified layer (orange curve in  
 260 figure 3). The resulting pair of modes have equal growth rates and opposite phase velocities.  
 261 They combine to form the oscillatory mode. As  $D \rightarrow \infty$ , the upper and lower instabilities  
 262 that form the oscillatory mode are independent, stationary KH modes with unequal phase  
 263 speeds.

264 We next explore the effects of varying  $Ri_0$  (figure 6). When  $D = 0$ , the stability boundary  
 265 for the two superimposed shear layers can be written as  $Ri_0 = 2k(1 - k)$ , neglecting viscosity  
 266 and assuming an infinite domain (e.g. Smyth & Carpenter 2019). This results in the instability  
 267 criterion  $Ri_0 < 1/2$ . Figure 6a depicts the growth rate in the  $k - Ri_0$  plane (Positive values

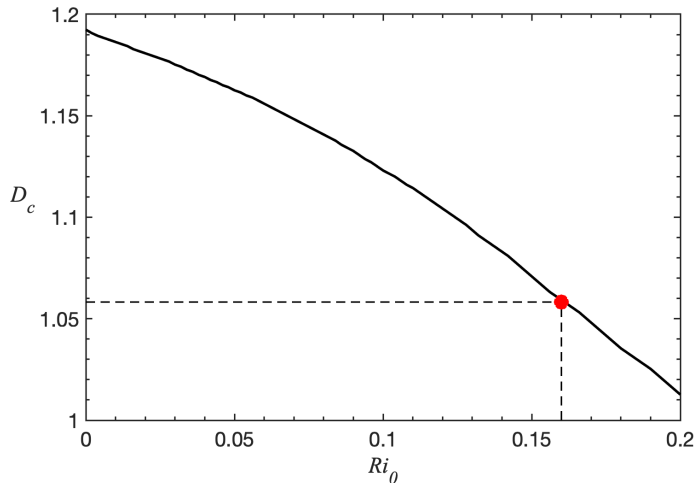


Figure 5: The dependence of critical distance  $D_c$  on  $Ri_0$ . The corresponding  $D_c$  for  $Ri_0 = 0.16$  is  $\sim 1.06$  as shown by the red dot.

268 lying outside the theoretical stability boundary are an artifact of the finite vertical domain  
 269 size; cf. Hazel 1972). The stationary mode dominates for  $D = 0$  and  $0.5$  (figure 6a and b).  
 270 As  $D$  increases from 0 to  $0.5$ , the unstable modes shift towards lower wavenumbers. When  
 271  $D = 1$ , the stationary mode is the fastest-growing mode, and its associated fastest-growing  
 272 wavenumber decreases to less than  $0.2$  for all  $Ri_0$  (figure 6c). At higher wavenumbers, the  
 273 oscillatory mode dominates. With an increase in  $D$  to  $3$ , the upper and lower shear layers  
 274 become widely separated, resulting in the disappearance of the stationary mode and the  
 275 dominance of the oscillatory mode (see figure 6d). The stability boundary under the inviscid  
 276 limit, depicted as the dashed curve, aligns well with the numerical results. This alignment  
 277 suggests that, at least within the linear regime, the configuration with  $D = 3$  resembles a pair  
 278 of isolated shear layers. To summarize, figure 6 shows that the modal structure in the linear  
 279 regime is remarkably insensitive to the choice of  $Ri_0$ ; at each  $D$  we see only the expected  
 280 decrease of growth rate with increasing  $Ri_0$ . In what follows, we will focus on the case  
 281  $Ri_0 = 0.16$ .

282 We next examine the vertical structures of typical stationary and oscillatory modes. The  
 283 eigenfunction of the stationary mode at  $D = 0.5$  (figure 7a) displays symmetry about  $z = 0$ ,  
 284 characteristic of KH instability (e.g. Smyth & Peltier 1989). The corresponding phase speed  
 285 is zero (figure 7a). When  $D = 2$ , modes are associated with the upper and lower shear layers.  
 286 The corresponding eigenfunctions are reflections of each other about  $z = 0$  (figure 7b and c).  
 287 While upper and lower modes share identical growth rates  $\sigma_r$ , their phase speeds are equal  
 288 but opposite, so that their sum has an oscillatory, standing wave-like character.

289 To close this section, we discuss the mechanisms that cause growth rates to decrease as  
 290  $D$  approaches  $D_c$ . As  $D \rightarrow D_c$  from above, the oscillatory mode is damped. To explain, we  
 291 invoke the wave resonance mechanism for piecewise linear shear layers (Heifetz *et al.* 2004;  
 292 Heifetz & Guha 2019; Carpenter *et al.* 2013; Smyth & Carpenter 2019). The schematic  
 293 representation in figure 8a shows a piecewise linear velocity profile with four kinks (i.e.  
 294 vorticity discontinuities). Correspondingly, figure 8b depicts the vorticity wave associated  
 295 with each kink, showing phase-locking between wave 1 and wave 2, as well as between wave  
 296 3 and wave 4, each in the phase configuration that is optimal for resonant amplification.  
 297 This results in the growth of two trains of KH billows, corresponding to the oscillatory

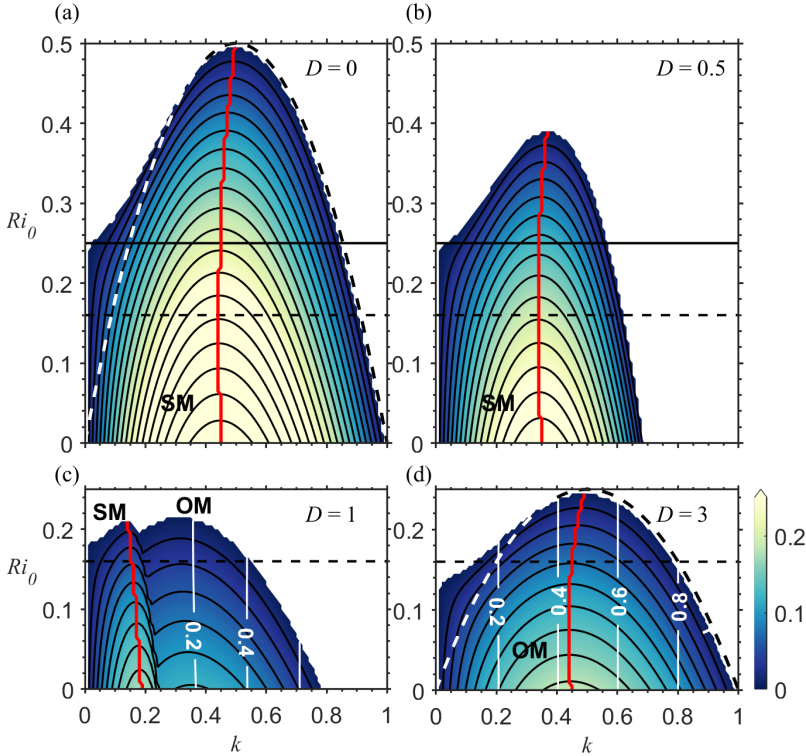


Figure 6: Stability diagram illustrating the transition from the stationary mode (SM) to oscillatory mode (OM) as  $D$  increases, with  $Re = 1000$ ,  $Pr = 1$ , and boundaries at  $z = \pm L_z/2 = \pm 15$ . Colours and black contours represent the growth rate on the  $k - D$  plane for different values of  $D$ : (a)  $D = 0$ , (b)  $D = 0.5$ , (c)  $D = 1$ , and (d)  $D = 3$ . The fastest growth rate at each  $k$ ,  $Ri_0$  is shown. The contour interval is 0.02. White contours represent the corresponding frequency  $\sigma_i$ . The red curve denotes the fastest-growing mode at each  $Ri_0$ . Dashed curves show the inviscid stability boundary for an infinite domain,  $Ri_0 = 2k(1 - k)$  when  $D = 0$  in (a) and  $Ri_0 = k(1 - k)$  for the single tanh profile considered in (d). Horizontal dashed line and solid line show  $Ri_0 = 0.16$  and  $Ri_0 = 0.25$ , respectively.

298 instability discussed above. When  $D$  is finite, an added interaction occurs between wave 2  
 299 and wave 3. (Interactions between waves 1 and 3, 2 and 4, and 1 and 4 are present but weaker  
 300 when  $D > D_c$ .) The phase relationship between these waves now varies in time, owing  
 301 to their opposing horizontal propagation. Figure 8b provides an example. In this particular  
 302 configuration, wave 2 and wave 3 force each other in their own directions. The opposite can  
 303 be true for other phase relationships that occur as the waves pass each other. Regardless of the  
 304 horizontal propagation, waves 2 and 3 consistently perturb each other's phases, so that they  
 305 cannot remain phase-locked in the optimal configuration for resonance, and the growth rate is  
 306 thus reduced. This destructive interference increases as  $D$  decreases until  $D = \tanh^{-1} \sqrt{1/3}$ ,  
 307 at which point the oscillatory mode vanishes, leaving only the stationary mode.

308 The damping we find as  $D \rightarrow D_c$  from below (figure 4) is unsurprising because the shear  
 309 maximum at  $z = 0$  weakens (figure 3b, compare dark blue and light blue curves), but it can  
 310 also be understood in terms of wave resonance. The resonance between wave 1 and wave 2,  
 311 as well as between wave 3 and wave 4, diminishes due to the disturbances between waves  
 312 2 and 3 described above. However, resonance between wave 1 and wave 4 remains strong,

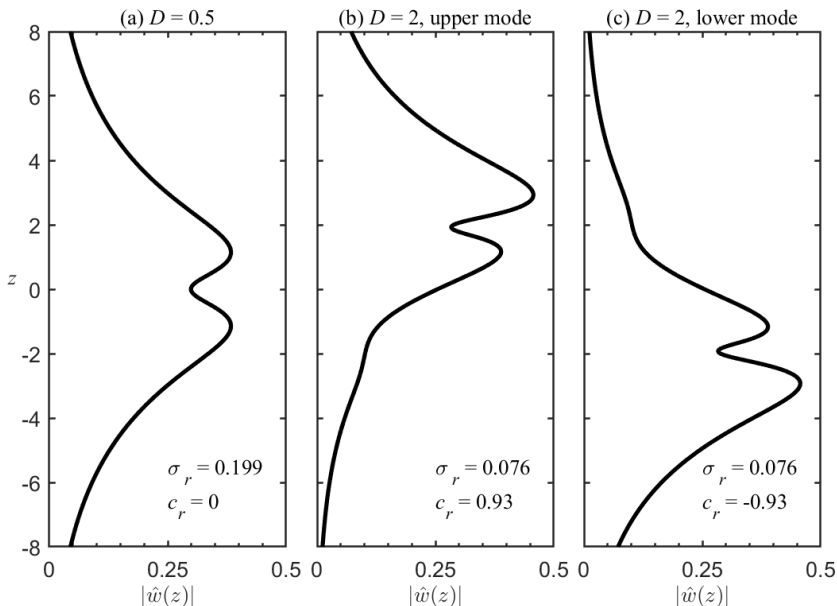


Figure 7: (a) Magnitudes of the vertical velocity eigenfunction  $\hat{w}$  for the fastest-growing mode when  $D = 0.5$ . This mode corresponds to a stationary KH-like instability. (b) and (c) depict the magnitudes of the vertical velocity eigenfunction for the upper and lower modes when  $D = 2$ . Both of these modes are oscillatory, exhibiting identical growth rates  $\sigma_r$  and phase speeds  $c_r$  of equal magnitude but opposite signs.

313 leading to the development of a KH-like instability. As  $D \rightarrow D_c^-$ , the separation between  
 314 wave 1 and wave 4 increases, rendering resonance less effective.

## 315 4. The Route to Turbulence

316

### 4.1. Overview of the Nonlinear Development

317 In this section, we look beyond the linear regime to examine the various secondary instabilities  
 318 that emerge at different separation distances  $D$  and trigger the transition to turbulence (see  
 319 examples in figure 9). In all cases, the initial condition consists of an unstable parallel shear  
 320 flow whose primary instability grows to form two-dimensional periodic laminar vortices.  
 321 These vortices attain maximum kinetic energy at  $t = t_{2d}$  (figure 9a, e, i). As expected, the  
 322 wavelength is largest (among these three examples) for  $D = 1$ , and smallest for  $D = 2$ ,  
 323 where two trains of billows combine to form the oscillatory instability (figure 9i). In the  
 324 oscillatory case  $D = 2$ , the growth rate and the time of turbulence onset are sensitive to  
 325 the details of the initial perturbations, as is evident in the contrast between the upper and  
 326 lower billow trains (figure 9i,j). The evolution progresses at a comparatively slower rate  
 327 for  $D = 1$ , consistent with its relatively small linear growth rate, while growth is faster  
 328 for  $D = 0.5$  (compare the value of  $t_{2d}$  between cases). During this progression, various  
 329 secondary instabilities emerge, facilitating the breakdown of the primary KH billows (e.g.  
 330 figure 9b, f, and j). This breakdown leads to the generation of turbulence (e.g. at  $t = t_{3d}$ ,  
 331 figure 9c, g, and k). Following the turbulent mixing phase, the flow relaminarizes (figure 9d,  
 332 h, l).

333 Secondary instabilities that govern the evolution of isolated KH billows at different values  
 334 of  $Ri_{min}$  have been explored in previous research (e.g. Davis & Peltier 1979; Klaassen &

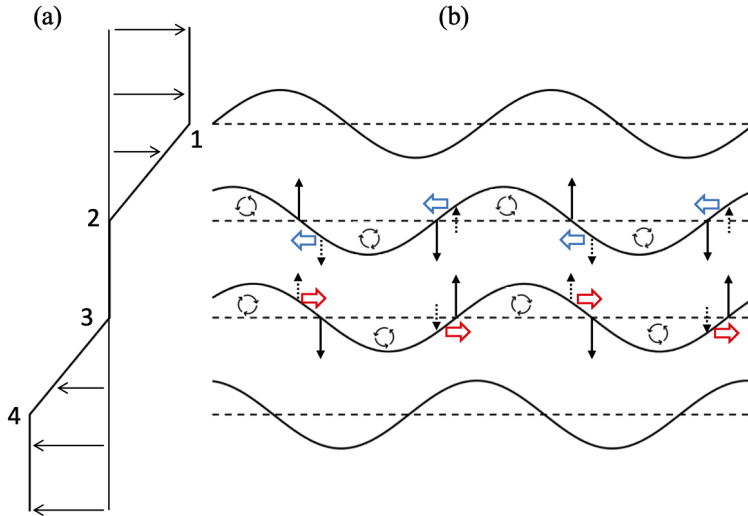


Figure 8: (a) Piece-wise linear background velocity profile. (b) Vorticity wave field diagram. Waves 1 and 2 resonate to create the upper KH-like instability. The phase difference  $0.35\pi$  is optimal for growth. The same is true for waves 3 and 4, which create the lower KH-like instability. The main interaction between these two instabilities involves waves 2 and 3. Counter-rotating vorticity perturbation causes alternately upward and downward motion (black solid arrows). These motions induce vertical motions to the nearby waves (black dashed arrows). Therefore, the interaction accelerates the upper wave to the left (blue arrows) and the lower wave to the right (red arrows).

335 Peltier 1985, 1991; Mashayek & Peltier 2012*a,b*, 2013, L22) . In sections §4.2 and §4.3,  
 336 we focus on secondary instabilities that contribute to 3-D perturbation kinetic energy in  
 337 the regimes  $D > D_c$  and  $D < D_c$ , wherein the linear development is dominated by the  
 338 oscillatory and stationary modes, respectively. Pertinent examples include the central core  
 339 instability (CCI, e.g. Klaassen & Peltier 1991, L23), which is catalyzed by the initial growth  
 340 of the KH instability, and the shear-aligned convective instability (SCI, e.g. Davis & Peltier  
 341 1979; Klaassen & Peltier 1985), which manifests when KH billows reach a sufficient size to  
 342 overturn the buoyancy structure. In §4.4, we discuss two-dimensional secondary instabilities:  
 343 the secondary shear instability of the braids (SSI) and pairing of adjacent billows (visible in  
 344 figures 9f and 9b, respectively).

345

#### 4.2. $D > D_c$

346 We examine the regime  $D > D_c$ , using ensembles of simulations with  $D \rightarrow \infty$ ,  $D = 3$ ,  
 347 and  $D = 2$  as examples. When the shear layers are infinitely separated ( $D \rightarrow \infty$ ), they are  
 348 independent of each other and each exhibits the standard KH instability (e.g. L22). The 3-D  
 349 perturbation kinetic energy  $\mathcal{K}_{3d}$  (figure 10a) is mostly created by shear production  $\mathcal{R}_{3d}$ ,  
 350 which draws energy from the mean flow (blue curve). The growth of  $\mathcal{R}_{3d}$  can be attributed  
 351 to the sinusoidal distortion of the spanwise vortex tube at the core of each nascent KH billow,  
 352 which redirects spanwise ( $y$ ) vorticity towards the  $x - z$  plane. The tilt of the sinusoidal

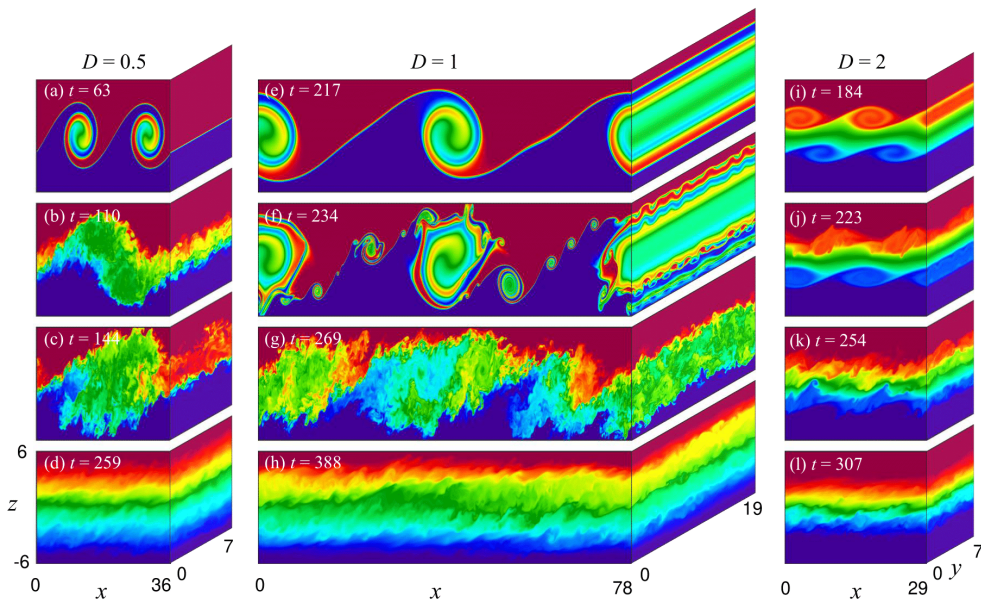


Figure 9: Cross-sections through the 3-D buoyancy field for example cases with  $D = 0.5$  (a)-(d),  $D = 1$  (e)-(h), and  $D = 2$  (i)-(l) at successive times as indicated. The buoyancy value plotted ranges from -1.5 (blue) to 1.5 (red). Snapshots in the first row (a, e, i) correspond to  $t = t_{2d}$ , the third row corresponds to  $t = t_{3d}$ , and the fourth row shows  $t = t_f$ , the time when  $\mathcal{M} = \mathcal{D}_p$ .

353 distortion is such that the Reynolds stress  $\langle u_{3d}w_{3d} \rangle_{xyz}$  becomes negative (see figure 14 of  
 354 Lasheras & Choi (1988), figure 9 of Smyth & Winters (2003) or figure 8 of Smyth (2006)).  
 355 This negative 3-D stress field works with the positive mean shear  $d\bar{U}/dz$  to generate 3-D  
 356 kinetic energy. By  $t = t_{\sigma_{3d}}$  (the time of maximum 3-D growth),  $d\bar{U}/dz$  is no longer a  
 357 maximum in the billow core, but the Reynolds stress is. Therefore, the dominant contributor  
 358 to energy growth, quantified by  $\mathcal{R}_{3d}$ , arises in this region. We identify this mode as CCI.

359 The buoyancy production  $\mathcal{H}_{3d}$  (red curve) is positive but much smaller than  $\mathcal{R}_{3d}$ . In  
 360 the current case with  $Ri_0 = 0.16$ , previous work suggests that SCI (signalled by positive  
 361  $\mathcal{H}_{3d}$ ) should be suppressed. Based on secondary stability analysis, SCI grows only when  
 362  $0.065 < Ri_0 < 0.13$  (Klaassen & Peltier 1991). The dominance of shear production  $\mathcal{R}_{3d}$  and  
 363 suppression of buoyancy production  $\mathcal{H}_{3d}$  when  $D \rightarrow \infty$  are also consistent with the findings  
 364 of Mashayek *et al.* (2013), particularly in their case  $Ri_0 = 0.16$ ,  $Re = 6000$ .

365 As the separation distance between two shear layers is decreased from infinity to values  
 366 approaching  $D_c$  (e.g. our examples  $D = 3$  and  $2$ ), interactions become evident. When  
 367  $D = 3$ , the evolution of each perturbation energy term resembles the infinite separation case  
 368 (compare figures 10a and 10b), suggesting only a weak interaction between the upper and  
 369 lower instabilities. When  $D = 2$ ,  $\mathcal{R}_{3d}$  remains the dominant term (i.e. the principal secondary  
 370 instability is still CCI); however, a reduction in  $\mathcal{H}_{3d}$  (figure 10c) is observed. At  $t = t_{\sigma_{3d}}$ , for  
 371 example, the reduction is  $\sim 40\%$  compared to case  $D \rightarrow \infty$ . This reduction can be attributed  
 372 to the close proximity of the shear layers, which results in additional suppression of SCI  
 373 beyond the inherent effects of high  $Ri_{min}$ . Because the upper and lower billows co-rotate,

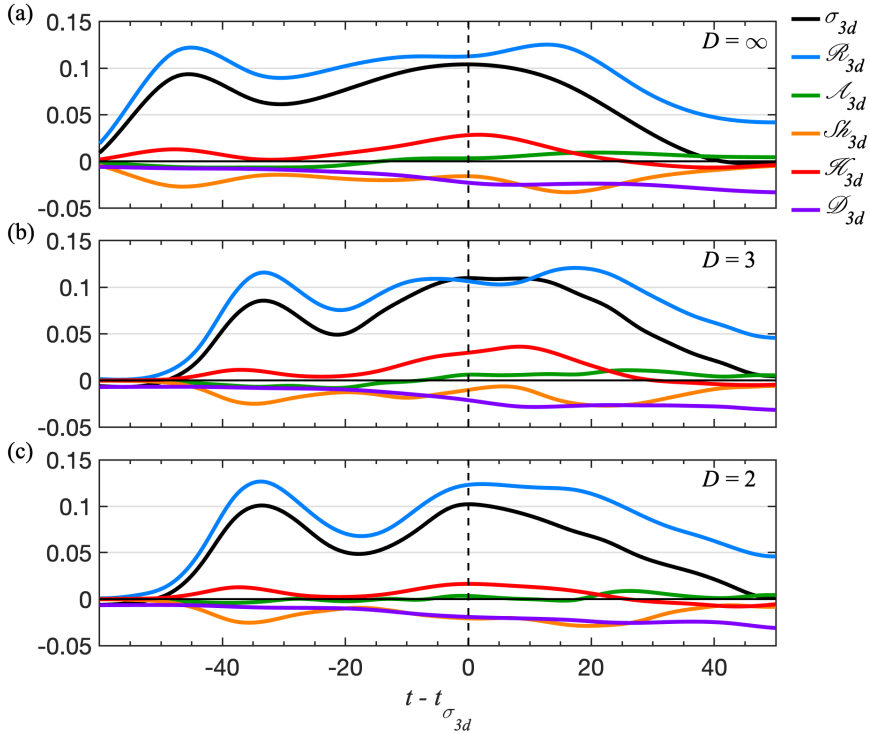


Figure 10: Time variation of terms of the  $\sigma_{3d}$  equation (2.21) when (a)  $D = \infty$ , (b)  $D = 3$ , and (c)  $D = 2$ . All curves are ensemble averaged. Vertical dashed lines show the time at which the growth  $\sigma_{3d}$  is a maximum. Note that the time for each ensemble case is shifted, such that the 3-D growth rate  $\sigma_{3d}$  is a maximum at  $t - t_{\sigma_{3d}} = 0$ . Terms except for  $\sigma_{3d}$  are obtained from cubic spline fits.

374 roll-up is suppressed, reducing overturning. This is reminiscent of the effect of a nearby  
 375 boundary on SCI (L23).

376

#### 4.3. $D < D_c$

377 We now examine distinctions that arise when  $D < D_c$ , using examples  $D = 0, 0.5$  and 1.  
 378 When  $D = 0$ , the two shear layers add to form a single shear layer with  $Ri_{min} = Ri_0/2 = 0.08$ .  
 379 Thus, the instability behaves similarly to a weakly-stratified shear instability, and we expect to  
 380 encounter SCI. During the earliest stage of 3-D growth ( $t - t_{\sigma_{3d}} \sim -18$  to  $-6$ ) the  $\mathcal{H}_{3d}$  budget  
 381 is dominated by the shear production term  $\mathcal{R}_{3d}$  due to CCI. By  $t \sim t_{\sigma_{3d}}$ , the billow has  
 382 rolled up enough to form convectively unstable layers. Consistent with the low initial  $Ri_{min}$ ,  
 383 SCI is now the principal secondary instability that breaks down the KH billow structure.  
 384 This is indicated in the  $\mathcal{H}_{3d}$  budget (figure 11) by increased values of  $\mathcal{H}_{3d}$  as well as  $\mathcal{S}h_{3d}$   
 385 and  $\mathcal{A}_{3d}$ . One would expect the buoyancy production term  $\mathcal{H}_{3d}$  to be substantial due to the  
 386 prevailing influence of SCI (Caulfield & Peltier 2000, L23). Surprisingly, both  $\mathcal{S}h_{3d}$  and  
 387  $\mathcal{A}_{3d}$  exhibit larger magnitudes than  $\mathcal{H}_{3d}$  (figure 11a). This finding is distinguished from  
 388 previous studies (Mashayek & Peltier 2013, L23), where buoyancy production dominated in  
 389 the presence of SCI. This may reflect a difference in the initial perturbations; the buoyancy  
 390 field was perturbed in the previous studies but not in the present work.

391 When  $D$  is slightly above 0 (typified here by  $D = 0.5$ ),  $Ri_{min}$  is small enough that the KH



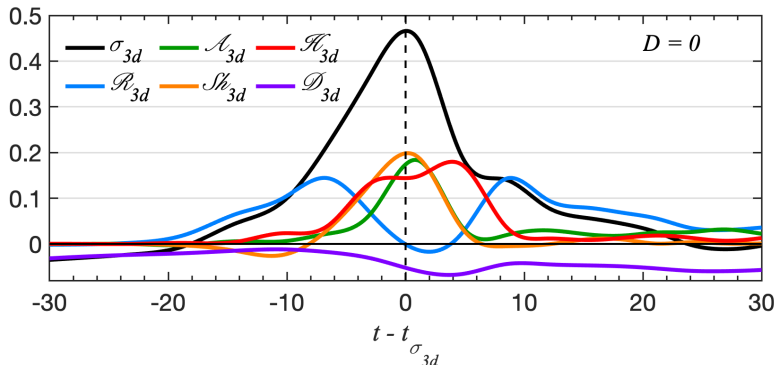


Figure 11: As in figure 10, but with  $D = 0$ .

392 billow is again susceptible to SCI (Klaassen & Peltier 1991). During the initial growth phase  
 393 (dot-dashed line in figure 12a), large positive values of  $\mathcal{R}_{3d}$  concentrate in the billow core,  
 394 indicating CCI. This mechanism can be discerned qualitatively in the spanwise-averaged  
 395  $x - z$  representation of  $\mathcal{R}_{3d}$  (figure 12b, region 1). Simultaneously, small areas of positive  
 396  $\mathcal{H}_{3d}$  manifest at the upper and lower extents of the billows (figure 12c, region 2). Moreover,  
 397 positive  $\mathcal{A}_{3d}$  emerges along the braids (figure 12d, region 3). These results are associated  
 398 with the mechanism illustrated in figure 12 of Lasheras & Choi (1988), who show that vortex  
 399 filaments present in the braids undergo amplification through stretching along the principal  
 400 plane of positive strain. These vortex filaments eventually envelop the spanwise vortex tubes  
 401 of the central core, resulting in positive  $\mathcal{H}_{3d}$  in the upper and lower regions of each billow  
 402 and positive  $\mathcal{A}_{3d}$  at the braids. Owing to the wrapping of these vortex filaments, the spanwise  
 403 vortex tubes undulate (figure 14 in Lasheras & Choi 1988), creating positive  $\mathcal{R}_{3d}$  in the core.  
 404 Nonetheless,  $\mathcal{H}_{3d}$  is mostly negative in the braids and in the billow cores, leading to an  
 405 overall negative volume average (dashed line in figure 12a). Positive  $\mathcal{H}_{3d}$  in the eyelids  
 406 (region 4 of figure 12e) indicates SCI.

407 At  $t = t_{\sigma_{3d}}$ , similar to  $D = 0$ ,  $\mathcal{H}_{3d}$  is smaller than both  $\mathcal{H}_{3d}$  and  $\mathcal{A}_{3d}$  (figure 12a). SCI  
 408 induces the formation of shear-aligned convective rolls, consistent with increased buoyancy  
 409 production  $\mathcal{H}_{3d}$  (figure 12i, region 7). Positive  $\mathcal{H}_{3d}$  coincides with these convective rolls  
 410 (region 5), suggesting that SCI could be responsible for its generation. During the early  
 411 growth phase,  $\mathcal{H}_{3d}$  (region 4) begins to increase on the eyelids of each billow, whereas  $\mathcal{H}_{3d}$   
 412 remains small or negative in that area (figure 12c). This implies that, as time progresses,  
 413 the increase in positive  $\mathcal{H}_{3d}$  on the eyelids results from the formation of shear-aligned  
 414 convective rolls with circulations tilted against the two-dimensional shear (figure 13). Vortex  
 415 tubes at the periphery of the billows also undergo stretching as quantified by  $\mathcal{A}_{3d}$ . Stretching  
 416 occurs when denser fluid descends on the upper right portion of the billow under the action  
 417 of gravity while lighter fluid ascends on the lower left (figure 12h, region 6).

418 During this phase of maximum growth, negative  $\mathcal{R}_{3d}$  emerges at the margins of the billows  
 419 (figure 12f). Consequently, the volume-averaged value is negative (figure 12a, indicated by  
 420 the blue curve at  $t = t_{\sigma_{3d}}$ ). This suggests that the background mean flow contributes little  
 421 to the 3-D perturbation kinetic energy in this instance. Instead, the perturbation energy is  
 422 partially created by buoyancy production but is predominantly due to shear production and  
 423 the stretching of vortex tubes as discussed above.

424 In the case  $D = 1$ , although the oscillatory mode is unstable, the dynamics are primarily  
 425 governed by the stationary mode. The perturbation energy terms evolve similarly to the case

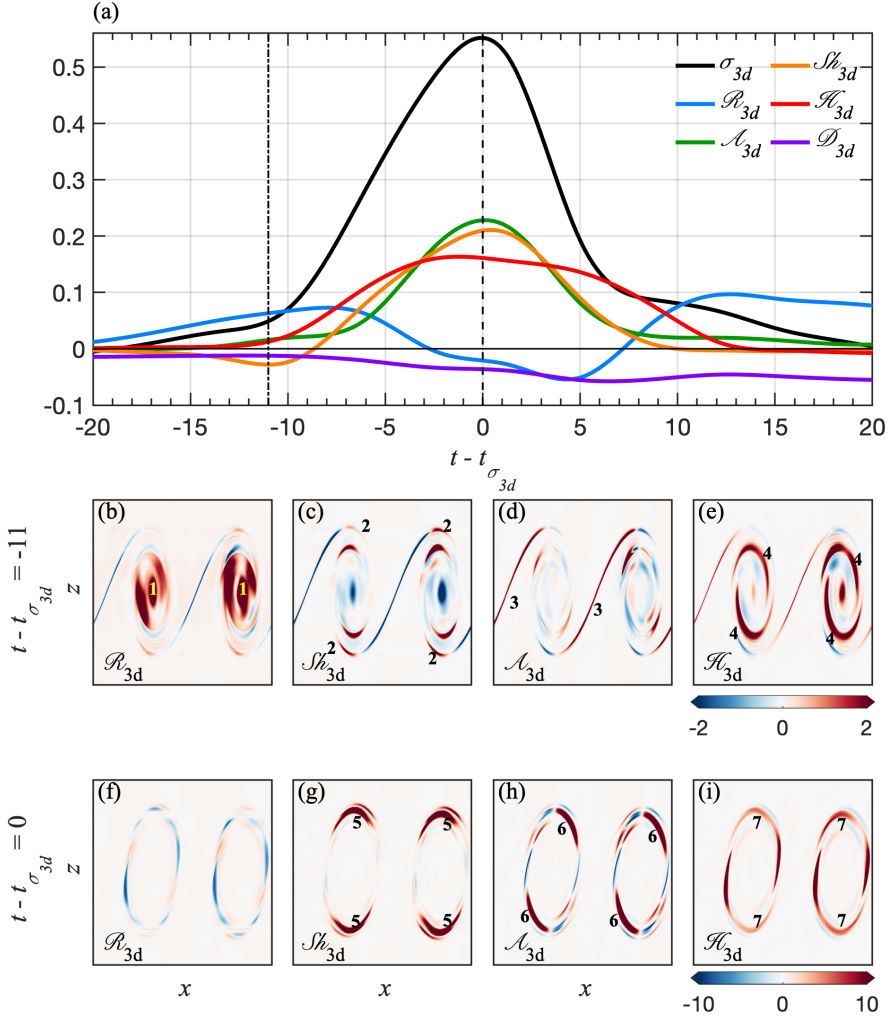


Figure 12: Dominant stationary mode when  $D = 0.5$ . (a) As in figure 10. Vertical dot-dashed line and dashed line show the time at  $t - t_{\sigma_{3d}} = -11$  and  $0$ , respectively. (b)-(e) shows spatial distribution of each energy terms:  $\mathcal{R}_{3d}$ ,  $\mathcal{S}\mathcal{h}_{3d}$ ,  $\mathcal{A}_{3d}$  and  $\mathcal{H}_{3d}$ , respectively, at  $t - t_{\sigma_{3d}} = -11$  (dot-dashed line in (a)). Same for (f)-(i) but at  $t - t_{\sigma_{3d}} = 0$  (dashed line in (a)).

426  $D = 0.5$  (compare figure 12a and figure 14). This is interesting because  $Ri_{min} = 0.15$ , which  
 427 is outside the range  $0.065 - 0.13$  where SCI is expected based on secondary stability analysis  
 428 of an isolated shear layer (Klaassen & Peltier 1991), yet the roll motions are visible, for  
 429 example, on the right face of figure 9f. We conclude that, as in the case  $D = 0.5$ , SCI gives  
 430 rise to shear-aligned convection rolls, consistent with positive values of  $\mathcal{H}_{3d}$ . The dominant  
 431 source terms are again  $\mathcal{S}\mathcal{h}_{3d}$  and  $\mathcal{A}_{3d}$  (figure 14).

432

#### 4.4. Secondary shear instability and pairing

433 We discuss secondary shear instability (SSI) and pairing separately as they affect  $\mathcal{H}_{3d}$   
 434 negligibly. SSI grows on the braids of the primary billows where the flow is nearly parallel  
 435 and the shear is intensified by the strain of the large billows (Corcos & Sherman 1976;

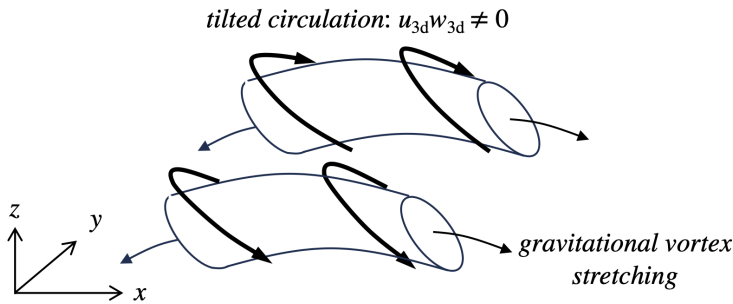


Figure 13: Schematic showing shear-aligned convective rolls tilting and stretching to form positive  $\mathcal{S}h_{3d}$  and  $\mathcal{A}_{3d}$ , respectively.

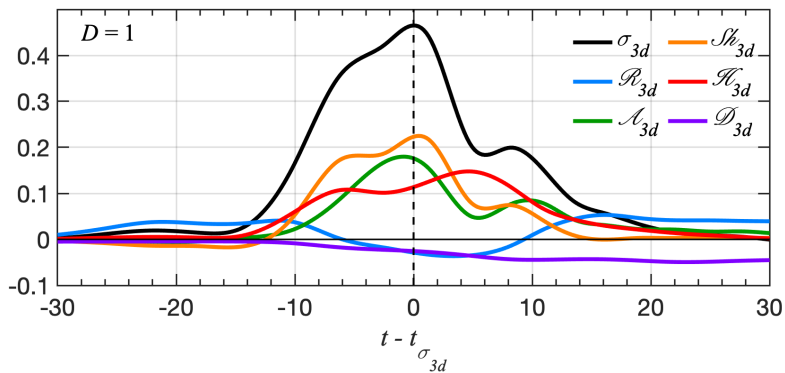


Figure 14: Dominant stationary mode when  $D = 1$ . As in figure 10.

436 Staquet 1995; Smyth 2003; Mashayek & Peltier 2012a). Staquet (1995) and Smyth (2003)  
 437 find that SSI tends to occur at higher  $Re_0$ . When  $D < D_c$  the initial mean flow resembles a  
 438 single shear layer with increased thickness and velocity change, i.e. with a larger Reynolds  
 439 number. Therefore, SSI may occur, depending on the initial noise field. An example is seen  
 440 in figure 9f. This secondary instability plays a notable role in generating turbulent mixing  
 441 (to be discussed in section §5). At  $t = t_{\sigma_{3d}}$ , when  $\sigma_{3d}$  is a maximum, the enstrophy of  
 442 the spanwise component  $\mathcal{Z}_y$  (figure 15b) is significantly stronger than that of the other two  
 443 components combined,  $\mathcal{Z}_x + \mathcal{Z}_z$  (figure 15a). The same is true for later times (figure 15c,d  
 444 in the SSI-affected region), further confirming the two-dimensional nature of SSI.

445 Secondary billows can be created either in pairs straddling the braid stagnation point or  
 446 individually (Smyth 2003), as seen at  $t - t_{\sigma_{3d}} = 7$  in figure 15d. Between the large billow  
 447 cores, a pair of smaller billows emerge at the stagnation point. The pair eventually merges  
 448 and becomes a larger single vortex, which then creates its own tertiary shear instability

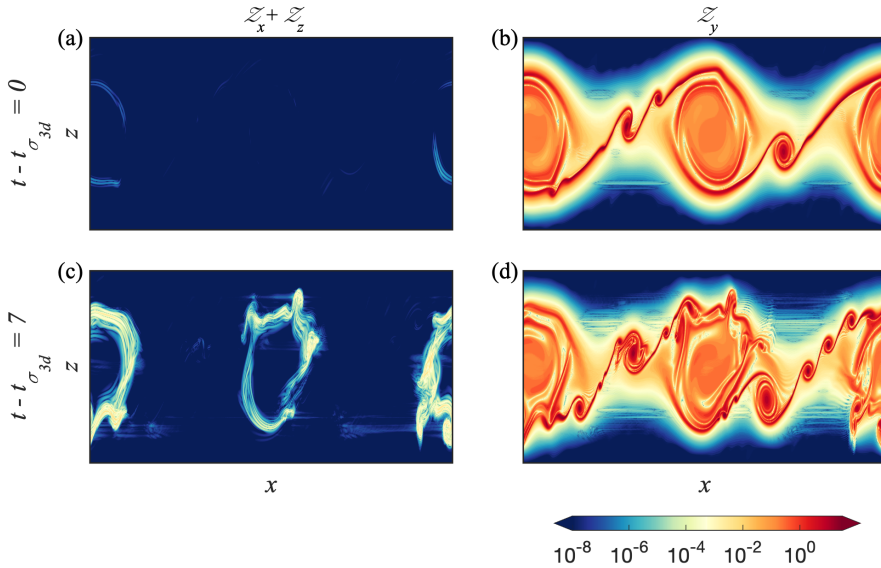


Figure 15: Spatial distribution of enstrophy during and after maximum secondary instability growth. Data are from a sample simulation in the  $D = 1$  ensemble. (a,c):  $x$  and  $z$  components combined; (b,d):  $y$  component. (a) and (b) are both at  $t - t_{\sigma_{3d}} = 0$ , and (c) and (d) are at  $t - t_{\sigma_{3d}} = 7$ .

449 in its surroundings, a vivid illustration of a self-similar downscale energy cascade. Other  
 450 secondary billows developed away from the stagnation point are advected outward by the  
 451 extensional strain.

452 Vortex pairing is also affected by a nearby shear layer. Pairing is more likely to occur when  
 453  $D$  is small (e.g.  $D = 0$  and  $0.5$ ), due to small  $Ri_{min}$  (figure 9b). L22 found that pairing is  
 454 laminar (i.e. it occurs prior to the onset of turbulence) in cases with  $Ri_{min}$  less than  $0.14$ ,  
 455 and we expected this to remain true in the present cases where  $Ri_{min}$  is considerably smaller.  
 456 However, figure 9c indicates turbulent pairing. This is likely due to the difference in shape  
 457 between the present shear layer and the single hyperbolic tangent profile assumed in L22.  
 458 When  $D \sim 0$ , pairing precedes the onset of SSI, leading to the disappearance of alternate  
 459 braids. Subsequently, if the braids are not yet turbulent, SSI is likely to appear. The timing  
 460 of turbulence onset, which itself depends on the choice of initial perturbation (L22), partly  
 461 determines the occurrence of pairing and SSI.

## 462 5. Turbulent Mixing

463 A neighbouring unstable shear layer could influence turbulent mixing through its impact on  
 464 the route to turbulence. We test this possibility by investigating three mixing properties: the  
 465 mixing rate  $\mathcal{M}$ , the dissipation rate  $\epsilon$ , and the mixing efficiency  $\eta$ , in both instantaneous  
 466 (figure 16) and cumulative (figure 18) forms.

### 467 5.1. Instantaneous Mixing Properties

468 We first examine cases with an isolated shear layer, namely,  $D = 0$  and  $D \rightarrow \infty$ , to set the  
 469 stage for cases with  $D \sim O(1)$ . When  $D = 0$ , mixing efficiency peaks as the billows roll up  
 470 ( $t \sim 60$ , black curve in figure 16c). At this pre-turbulent stage, the mixing rate is large (figure  
 471 16a) due to sharp scalar gradients while the dissipation rate (figure 16b) remains small, and

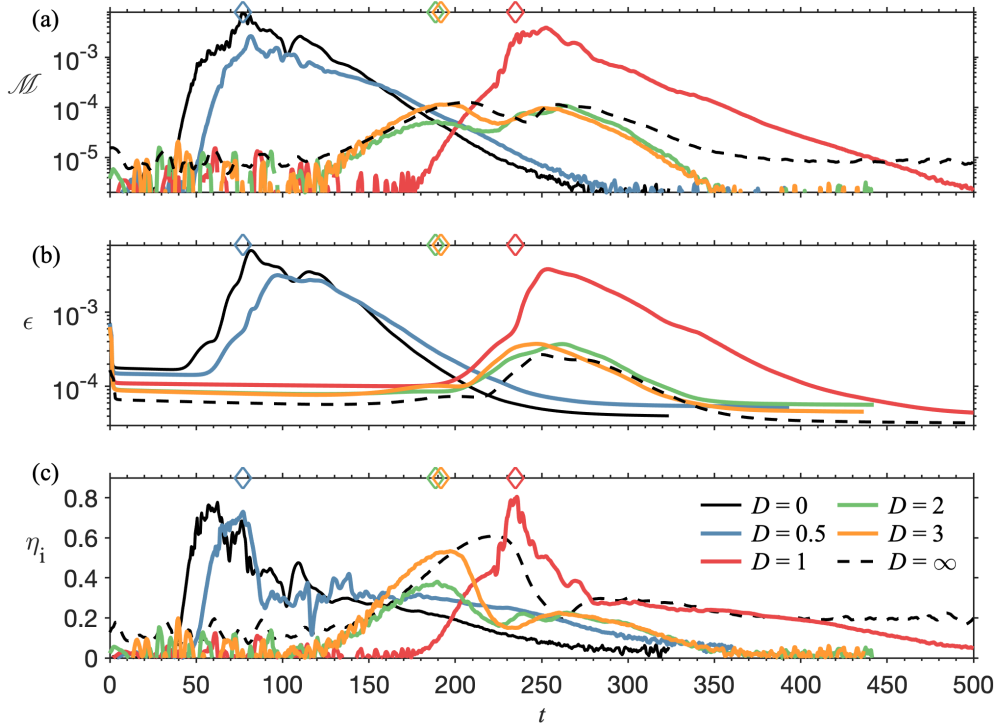


Figure 16: Time variation of the instantaneous (a) mixing rate, (b) total dissipation of the kinetic energy, and (c) mixing efficiency, with varying  $D$ . For clarity, only one ensemble member is included for each case of different  $D$ . Note that the magnitude and timing of the peak can be slightly different, but the overall trend is similar between each ensemble case.

The solid and dashed black curves are the case with the isolated shear layer. A running mean is carried out for all curves. Diamonds correspond to the snapshots in figure 17.

472 mixing efficiency is therefore large (Winters *et al.* 1995; Caulfield & Peltier 2000; Smyth &  
 473 Moum 2001; Smyth 2020). Subsequently, the billow structure collapses due to SCI (section  
 474 4), leading to an increase in both mixing and dissipation rates. Thus, mixing efficiency is  
 475 reduced at  $t \sim 70$  as the flow becomes turbulent. As the billows pair and merge into a single  
 476 large vortex ( $t \sim 110$ ), the mixing and dissipation rates begin to rise.

477 In the case  $D \rightarrow \infty$ ,  $Ri_{min}$  doubles to 0.16. Therefore, mixing is visibly weaker than at  
 478  $D = 0$  (compare black solid and dashed curves, figure 16a). However, since the dissipation  
 479 rate is also smaller, the peak mixing efficiency at  $t \sim 208$  ( $\eta_i = 0.63$ ) for  $D \rightarrow \infty$  is not  
 480 very different from the peak value for  $D = 0$  at  $t \sim 62$  ( $\eta_i = 0.78$ ). The two peaks of  
 481  $\mathcal{M}$  are associated respectively with the breakdown of the billow and with mixing due to  
 482 fully-developed turbulence (cf. Kaminski & Smyth 2019, L23).

483 When  $D = 0.5$ , the mixing characteristics resemble those at  $D = 0$ . Mixing efficiency  
 484 exhibits a peak during roll-up (as  $t = 76$ , marked by the blue diamond in figure 16c). Strong  
 485 mixing, quantified by the buoyancy variance dissipation rate  $\chi'$  (2.19), begins along the  
 486 braids and extends inward through overturned layers surrounding the core (figure 17a).

487 When  $D = 1$ , the time at which the billows roll up is the latest compared with other cases  
 488 of  $D$ , consistent with its smallest growth rate (figure 4). The increase of mixing efficiency  
 489 begins at  $t \sim 180$  (red curve in figure 16c). Subsequently, the mixing rate increases rapidly  
 490 due to the amplifying KH billow. At  $t = 217$ , the 2-D kinetic energy reaches its maximum,

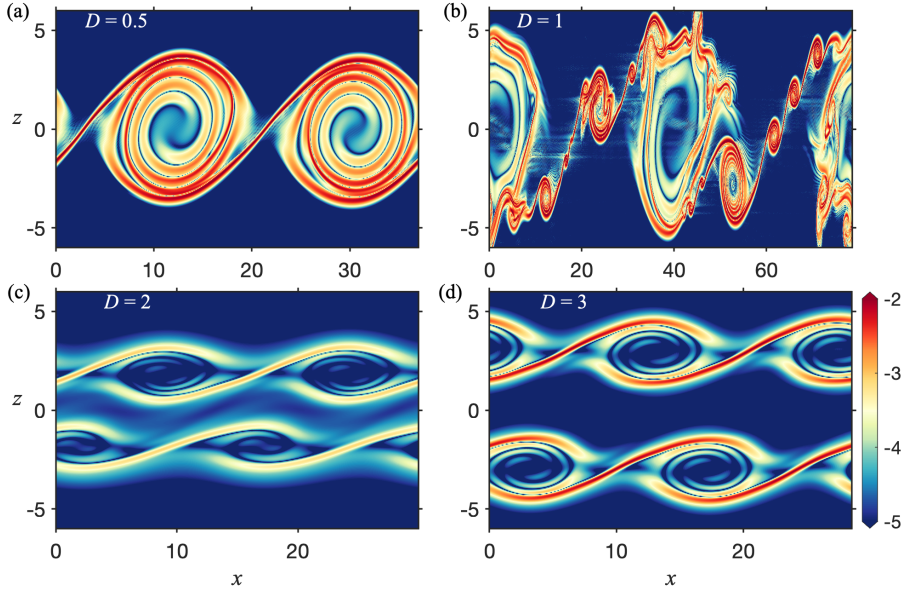


Figure 17:  $x - z$  slice of the buoyancy variance dissipation rate  $\log \chi'$  when the instantaneous mixing efficiency  $\eta_i$  is a maximum for (a)  $D = 0.5$ , (b)  $D = 1$ , (c)  $D = 2$ , and (d)  $D = 3$ . The snapshots for different  $D$  cases correspond to the diamond symbols in figure 16.

491 while dissipation remains relatively weak, accounting for the highly efficient mixing. Before  
 492 SCI collapses the KH billow structure, SSI emerges along the braids. The emergence of SSI  
 493 leads to a surge of highly efficient mixing ( $t = 215 - 235$  in figure 16a). Mixing is most  
 494 intense in the braids, where it coincides with the secondary KH billows (figure 17b), and is  
 495 most efficient at  $t = 235$  (red diamond) because the secondary billows have not yet become  
 496 turbulent, with  $\eta_i \sim 0.8$  (figure 16c).

497 The SSI billows travel along the braids toward the primary KH billow, and then intermingle  
 498 with the shear-aligned convective rolls at the eyelids (at  $x = 40$ , figure 17b). The primary  
 499 KH billow then collapses and the flow becomes more turbulent ( $t \sim 250$ ). At this time, the  
 500 mixing and dissipation rates approach their peak values, coinciding with a precipitous drop  
 501 in the mixing efficiency (figure 16c).

502 The regime  $D > D_c$ , in which the oscillatory instability dominates (§3), is typified here  
 503 by the cases  $D = 2$  and  $D = 3$ . Both the mixing rate and dissipation rate are weak compared  
 504 to cases where stationary mode dominates, e.g.  $D = 0, 0.5$  and  $1$  (figure 16a and b). This  
 505 weakening is due to the stronger stratification which tends to damp both SCI and pairing.  
 506 In addition, the mutual interference of neighbouring billows suppresses the growth of the  
 507 primary KH instability, leading to reduced overturning and 3-D convection, hence smaller  
 508  $\mathcal{M}$  (compare  $D = 2$  and  $D = \infty$  in figure 18a).

509 While the general pattern of mixing, dissipation, and mixing efficiency remains largely  
 510 consistent across all cases when  $D > D_c$ , there is a reduction in mixing efficiency as  $D \rightarrow D_c^+$   
 511 (compare peak values for  $D = \infty$ ,  $D = 3$  and  $D = 2$  in figure 16c). This reduction mainly  
 512 reflects the diminished mixing rate  $\mathcal{M}$  observed at smaller values of  $D$ . As shown in figure  
 513 17c and d,  $\chi'$  is less pronounced in case  $D = 2$  compared to case  $D = 3$ . This suggests that,

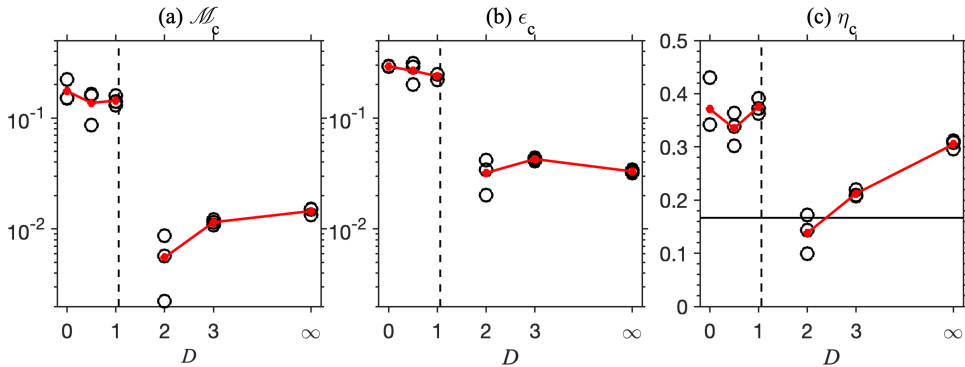


Figure 18: Dependence of (a) cumulative mixing, (b) cumulative dissipation, and (c) cumulative mixing efficiency on  $D$ . All ensemble cases are plotted. Red curves are the ensemble mean. The end time for the time integral is when  $\mathcal{M} = \mathcal{D}_p$ . The vertical dashed lines denote the critical separation distance  $D_c$ . The horizontal line denotes the canonical  $\eta_c = 1/6$  suggested by Osborn (1980).

514 as the nonlinear interaction between the upper and lower shear layers intensifies, mixing is  
515 suppressed.

516

### 5.2. Cumulative Mixing Properties

517 We next investigate the dependence of the cumulative mixing ( $\mathcal{M}_c$ ), dissipation ( $\epsilon_c$ ), and  
518 mixing efficiency ( $\eta_c$ ), on the separation distance  $D$ . When  $D < D_c$ , the net mixing and  
519 dissipation are  $\sim 1$  order of magnitude larger than when  $D > D_c$  (figure 18a and b). There is  
520 less disparity in  $\eta_c$ , indicating an approximate balance between mixing and dissipation that  
521 tends to preserve mixing efficiency. Even so, mixing is typically more efficient by a factor  
522  $\sim 2$  when  $D < D_c$  compared to when  $D > D_c$ . At the extremes  $D = 0$  and  $D \rightarrow \infty$ ,  $\eta_c$  takes  
523 the high values (0.3-0.4) expected for an isolated shear layer (Winters *et al.* 1995; Caulfield  
524 & Peltier 2000; Smyth *et al.* 2001).

525 In the oscillatory regime, the overall reduction in total amount of mixing as  $D$  approaches  
526  $D_c$  from above may be attributed to the suppression of both the primary KH instability  
527 (due to interference between neighbouring billows impeding the phase-locking of resonant  
528 waves, as discussed in Section 3) and secondary instabilities. SCI, which plays a major  
529 role in driving mixing, can be impacted both by the reduced overturning in the suppressed  
530 primary KH instability and the neighbouring effect (§4.2). This suppression of SCI becomes  
531 more pronounced as  $D \rightarrow D_c^+$ , potentially leading to a complete prevention of mixing –  
532 auxiliary simulations with  $D = 1.5$ , not shown here, failed to generated detectable instability  
533 or mixing. While  $\mathcal{M}_c$  decreases as  $D \rightarrow D_c^+$ , there is little corresponding change in total  
534 dissipation (figure 18b), leading to an overall decrease in mixing efficiency.

535 In the stationary regime  $D < D_c$ , there is a slight tendency toward stronger mixing and  
536 dissipation (figure 18a and b) with decreasing  $D$ . This is likely associated with the slight  
537 reduction of  $Ri_{min}$ .

538

### 5.3. Emergence of Marginal Instability

539 Geophysical stratified shear flows are often in a state of marginal instability (MI), wherein  
540 the mean flow fluctuates around a stability boundary approximated by  $Ri_g = 1/4$  (see Smyth  
541 2020, for a recent review). In the present simulations, we find MI-like behaviour when  $D = 2$   
542 (figure 19b,e,h). As turbulence decays ( $t \sim 250$ ), a layer of near-critical  $Ri_g$  (i.e. clustered

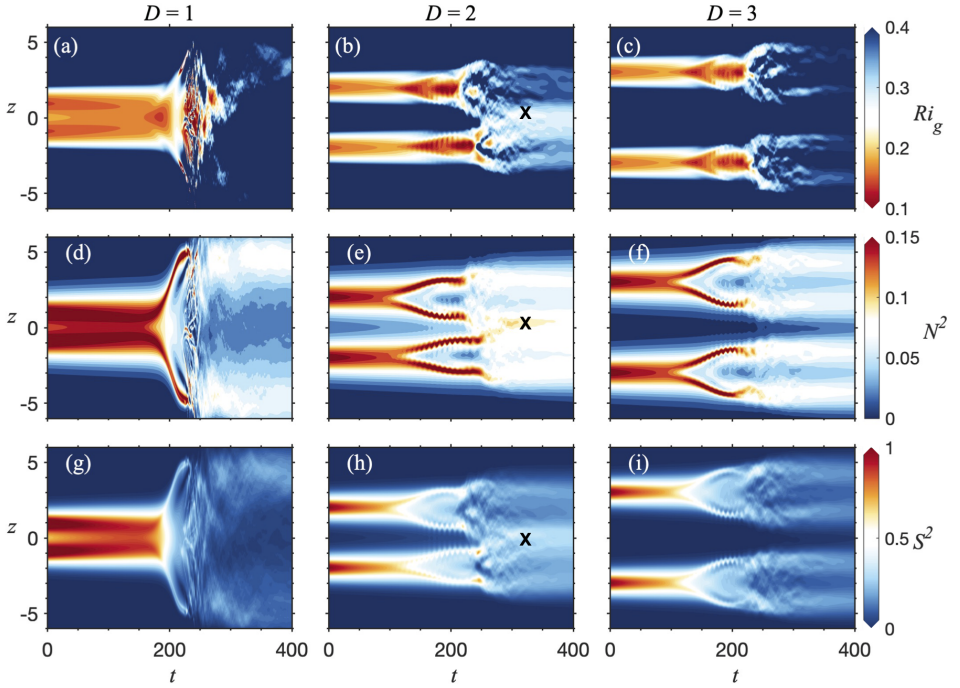


Figure 19: Horizontally averaged time series of  $Ri_g$  (a)-(c),  $N^2$  (d)-(f), and  $S^2$  (g)-(i). The symbol  $\times$  indicates the potential location for marginal instability to occur.

543 around a value near  $1/4$ ) emerges around  $z = 0$  (figure 19b, symbol  $\times$ ). This near-critical  
 544  $Ri_g$  corresponds to a new stratified shear layer that forms between the two original layers  
 545 (figures 19e and h) as mixing brings fluid from the upper and lower turbulent layers into  
 546 close contact in the middle region, leading to local amplification of the mean buoyancy and  
 547 velocity gradients.

548 MI appears only in a restricted range of  $D$ , namely when the instability is in the oscillatory  
 549 regime ( $D > D_c$ ) but  $D$  is not much greater than  $D_c$ . Conversely, for  $D < D_c$ , the mixing  
 550 characteristics resemble those of a typical KH instability, where both stratification and shear  
 551 are smoothed due to strong overturning (figure 19d,g). This leads to an increase of  $Ri_g$   
 552 towards a stable state (figure 19a). When  $D$  is much greater than  $D_c$ , e.g.  $D = 3$ , the upper  
 553 and lower shear layers remain too distant to overlap despite their expansion. Consequently,  
 554 the weakly-stratified and weakly-sheared middle layer (at  $z = 0$ ) persists (figure 19f,i) such  
 555 that  $Ri_g$  is much greater than  $1/4$  (figure 19c).

## 556 6. Summary

557 We have investigated the instabilities of a pair of shear layers. When the layers are either  
 558 unseparated or separate to an infinite extent, flow evolution is driven by the classical KH



559 instability. Our primary focus, however, is cases characterized by a finite, nonzero separation  
560 distance  $D$ .

561 In the small-amplitude limit we find two distinct regimes: (1) a stationary mode, defined  
562 by a unique maximum growth rate, dominates when  $D < D_c$  (where  $D_c \approx 1$  is the critical  
563 separation distance) and (2) an oscillatory mode, consisting of two modes with equal growth  
564 rates and different phase speeds, becomes unstable when  $D > \tanh^{-1} \sqrt{1/3}$  and dominates  
565 when  $D > D_c$ . As  $D \rightarrow D_c$  from below, the stationary mode is damped because the shear  
566 maximum weakens. As  $D \rightarrow D_c$  from above, damping of the oscillatory mode can be  
567 understood in terms of the resonant interaction of vorticity waves.

568 The presence of a neighbouring shear layer alters mixing and its efficiency by introducing  
569 an alternative route to turbulence. We have extended our analysis beyond the linear regime  
570 by conducting an ensemble of three direct numerical simulations, with different initial  
571 perturbations, for each of five values of the separation distance  $D$ . The presence of a  
572 neighbouring shear layer exerts a profound influence on the evolution and wavelength of the  
573 primary instability as well as the amplitude of the resulting KH billows. The KH instability  
574 evolves most rapidly when  $D$  is close to 0, consistent with its largest growth rate. As  $D$   
575 increases from 0 to  $D_c$ , the evolution of the instability is prolonged (consistent with its  
576 decreasing growth rate), and the wavelength and amplitude of the KH billows increase. As  
577  $D$  increases further from  $D_c$  to infinity, the evolution time and wavelength of the instability  
578 converge to values characteristic of an isolated shear layer.

579  $Ri_{min}$  is higher in the oscillatory regime ( $D > D_c$ ) and lower in the stationary regime  
580 ( $D < D_c$ ). Important differences in both the route to turbulence and the resulting mixing can  
581 be traced back to this distinction. In the oscillatory regime,  $Ri_{min} \approx Ri_0$ , SCI is suppressed  
582 due both to the influence of stratification (Klaassen & Peltier 1991) and to interference from  
583 the adjacent shear layer. CCI is now dominant. Mixing is relatively weak and inefficient.  
584 When the separation between the upper and lower shear layers is sufficiently small, a new  
585 shear layer, exhibiting MI, forms between them.

586 In the stationary regime ( $D < D_c$ ),  $Ri_{min}$  is lower and the instability resembles a weakly-  
587 stratified KH instability with large amplitude. SCI creates shear-aligned convective rolls,  
588 leading to an increase in buoyancy production (similar to previous studies, e.g. Caulfield  
589 & Peltier 2000, L23). Additionally, owing to weak stratification, billows are likely to pair.  
590 As  $D$  approaches  $D_c$  from below, buoyancy production becomes less important while shear  
591 production and gravitational stretching take over as the primary mechanisms of 3-D growth.  
592 SSI, while not contributing directly to 3-D perturbation kinetic energy, plays a significant  
593 role in generating turbulence.

594 The stationary mode leads to strong and efficient mixing. At the transition to the oscillatory  
595 regime, the cumulative mixing rate, dissipation rate and mixing efficiency all decrease  
596 abruptly (figure 18c), showing that mixing properties can be sensitive to small changes in  
597 the initial mean flow.

## 598 7. Future Directions

599 In this study, the initial parameters  $Ri_0$ ,  $Re_0$ , and  $Pr$  remain constant, with our primary  
600 focus on the impact of separation distances. Changing these parameters will alter the  
601 transition process in various ways. For example, a different  $Ri_0$  may alter the growth of  
602 KHI, subharmonic instability and 3-D secondary instabilities. Turbulent mixing and the  
603 potential for marginal instability would consequently be affected in ways that are difficult to  
604 anticipate. Moreover, varying  $Ri_0$  while fixing  $Ri_{min}$  could isolate the effect of the separation  
605 distance  $D$ .

606 Increasing  $Re_0$  is essential for simulating geophysical flows. This increase introduces a

607 variety of secondary instabilities, which could be affected by the presence of a neighbouring  
608 shear instability. The increase of  $Re_0$  facilitates exploration of approaching to the critical  
609 separation distance ( $D \sim D_c$ ), as the KH instability may transition to turbulence even when  
610 heavily damped by a neighbouring instability.

611 While  $Pr = 1$  is applicable to air, higher values are more realistic for water. A higher  
612  $Pr$  opens the possibility of a Holmboe-like instability when the mean buoyancy changes  
613 more abruptly with height than does velocity. Future studies will explore interactions of  
614 nearby Holmboe instability. This may give rise not only to KH-like instability (involving  
615 vorticity wave interaction) and Holmboe-like instability (involving vorticity and gravity  
616 wave interaction) but also to Taylor-Caulfield instability (interaction between two gravity  
617 waves, see Lee & Caulfield 2001; Smyth & Carpenter 2019), depending on the separation  
618 distance. Moreover, the scouring motion induced by Holmboe waves could be affected by  
619 the adjacent shear instability.

620 The variability in mixing parameters at varying separation distances has significant impli-  
621 cations for the estimation of mixing in geophysical flows, particularly those characterized by  
622 the presence of neighbouring shear instabilities (e.g. Desaubies & Smith 1982; Moum *et al.*  
623 2011). For the parameter values used here, the mixing efficiency ranges from  $\sim 0.14$  to  $\sim 0.37$ ,  
624 depending on the separation distance (figure 18c). Under different initial parameters or varied  
625 profile structures, such as asymmetrical velocity and buoyancy profiles (e.g. Olsthoorn *et al.*  
626 2023), the resulting mixing could also be substantially affected by a neighbouring instability.

627 The exploration of the parameter space will ultimately support a comprehensive parame-  
628 terization framework for capturing the influence of neighbouring shear layers in a larger-scale  
629 model. A future goal is to explore these effects in a multi-layer context, such as the interaction  
630 of breaking internal waves at ocean ridges and seamounts.

631 Pre-existing turbulence exerts a substantial influence on KH instabilities (Brucker & Sarkar  
632 2007; Kaminski & Smyth 2019). Furthermore, the onset timing of shear-driven turbulence  
633 is inherently arbitrary, making the simultaneous instability of two adjacent shear layers an  
634 atypical scenario. This highlights the potential impact of a near-field turbulent event on  
635 pre-turbulent shear instabilities. Such events may alter the development of turbulence in an  
636 adjacent shear layer.

637 Forced stratified flows may organize into layers consisting of neighbouring strongly  
638 stratified interfaces separated by regions of weak stratification, and a significant effort has  
639 been made to understand the circumstances under which these layers form and survive  
640 (Caulfield 2021; Petropoulos *et al.* 2023). While layered structures may be robust in certain  
641 scenarios, particularly in high- $Pr$  and double-diffusive flows (Timmermans *et al.* 2008; Taylor  
642 & Zhou 2017), in other scenarios they are prone to destruction by shear. Recent efforts have  
643 described, for example, the interaction between double-diffusive staircase structures and  
644 shear-driven turbulence (e.g. Bebieva & Speer 2019; Brown & Radko 2022). In the present  
645 problem, increasing the number of layers could provide insight into the development of  
646 turbulence in these multilayered flows.

647 **Acknowledgements.** This paper is part of the first author's Ph.D. thesis at Oregon State University. We  
648 appreciate useful input from advisory committee members Jim Moum, Jim Liburdy, Jonathan Nash and  
649 Brodie Pearson. We appreciate Jeff Carpenter's advice on the damping of the oscillatory mode (figure 8)  
650 and John Taylor's work in creating and curating DIABLO. The paper has benefited from the comments  
651 of the editor and the reviewers. We acknowledge high-performance computing support on Cheyenne  
652 (doi:10.5065/D6RX99HX) provided by NCAR's Computational and Information Systems Laboratory,  
653 sponsored by the U.S. National Science Foundation.

- 654 **Funding.** This work was funded by the US National Science Foundation under grant OCE-1830071. AKK  
655 was supported as the Ho-Shang and Mei-Li Lee Faculty Fellow in Mechanical Engineering at UC Berkeley.
- 656 **Declaration of interests.** The authors report no conflict of interest.
- 657 **Data availability statement.** DIABLO is available at <https://github.com/johnryantaylor/DIABLO>. Output  
658 data is available by request to the corresponding author.
- 659 **Author ORCIDs.** C.-L. Liu, <https://orcid.org/0000-0001-5134-7993>; A. K. Kaminski, <https://orcid.org/0000-0002-4838-2453>; W. D. Smyth, <https://orcid.org/0000-0001-5505-2009>.

## REFERENCES

- 661 ALFORD, MATTHEW H & PINKEL, ROBERT 2000 Observations of overturning in the thermocline: The context  
662 of ocean mixing. *Journal of Physical Oceanography* **30** (5), 805–832.
- 663 BEBIEVA, YANA & SPEER, KEVIN 2019 The regulation of sea ice thickness by double-diffusive processes in  
664 the Ross Gyre. *J. Geophys. Res. Oceans* **124**, 7068–7081.
- 665 BROWN, JUSTIN & RADKO, TIMOUR 2022 Disruption of Arctic staircases by shear. *Geophys. Res. Lett.* **49**,  
666 e2022GL100605.
- 667 BRUCKER, K. & SARKAR, S. 2007 Evolution of an initially turbulent stratified shear layer. *Phys. Fluids* **19**,  
668 105105.
- 669 CARPENTER, J.R., TEDFORD, E.W., HEIFETZ, E. & LAWRENCE, G.A. 2013 Instability in stratified shear flow:  
670 Review of a physical interpretation based on interacting waves. *Applied Mechanics Reviews* **64** (6),  
671 060801.
- 672 CAULFIELD, C.P. 2021 Layering, instabilities, and mixing in turbulent stratified flows. *Ann. Rev. Fluid Mech.*  
673 **53** (1), 113–145.
- 674 CAULFIELD, C.P. & PELTIER, W.R. 2000 Anatomy of the mixing transition in homogeneous and stratified  
675 free shear layers. *J. Fluid Mech.* **413**, 1–47.
- 676 CHANG, MING-HUEI, CHENG, YU-HSIN, YEH, YU-YU, YANG, YIING JANG, JAN, SEN, LIU, CHIH-LUN,  
677 MATSUNO, TAKESHI, ENDOH, TAKAHIRO, TSUTSUMI, EISUKE, CHEN, JIA-LIN & OTHERS 2022 Internal  
678 hydraulic transition and turbulent mixing observed in the kuroshio over the i-lan ridge off northeastern  
679 taiwan. *Journal of Physical Oceanography* **1** (aop).
- 680 CORCOS, G.M. & SHERMAN, F.S. 1976 Vorticity concentration and the dynamics of unstable free shear  
681 layers. *J. Fluid Mech.* **73**, 241–264.
- 682 DAVIS, P.A. & PELTIER, W.R. 1979 Some characteristics of the Kelvin-Helmholtz and resonant overreflection  
683 modes of shear flow instability and of their interaction through vortex pairing. *J. Atmos. Sci.* **36** (12),  
684 2394 – 2412.
- 685 DESAUBIES, YVES & SMITH, WOOLLCOTT K 1982 Statistics of richardson number and instability in oceanic  
686 internal waves. *Journal of Physical Oceanography* **12** (11), 1245–1259.
- 687 FRITTS, DAVID C, BAUMGARTEN, GERD, PAUTET, P-DOMINIQUE, HECHT, JAMES H, WILLIAMS, BIFFORD P,  
688 KAIFLER, NATALIE, KAIFLER, BERND, KJELLSTRAND, C BJORN, WANG, LING, TAYLOR, MICHAEL J &  
689 OTHERS 2023 Kelvin helmholtz instability “tube” & “knot” dynamics, part i: Expanding observational  
690 evidence of occurrence and environmental influences. *Journal of the Atmospheric Sciences* .
- 691 FRITTS, DAVID C, BIZON, CHRIS, WERNE, JOSEPH A & MEYER, CHRISTIAN K 2003 Layering accompanying  
692 turbulence generation due to shear instability and gravity-wave breaking. *Journal of Geophysical*  
693 *Research: Atmospheres* **108** (D8).
- 694 GEYER, W.R., LAVERY, A., SCULLY, M.E. & TROWBRIDGE, J.H. 2010 Mixing by shear instability at high  
695 Reynolds number. *Geophys. Res. Lett.* **37**, L22607.
- 696 GREGG, M.C., D’ASARO, E.A., RILEY, J.J. & KUNZE, E. 2018 Mixing efficiency in the ocean. *Ann. Rev.*  
697 *Marine Sci.* **10** (1), 443–473.
- 698 HAZEL, P. 1972 Numerical studies of the stability of inviscid parallel shear flows. *J. Fluid Mech.* **51**, 39–62.
- 699 HEIFETZ, E., BISHOP, C. H., HOSKINS, B. J. & METHVEN, J. 2004 The counter-propagating rossby-wave  
700 perspective on baroclinic instability. i: Mathematical basis. *Q. J. R. Meteorol. Soc.* **130**, 211–231.
- 701 HEIFETZ, EYAL & GUHA, ANIRBAN 2019 Normal form of synchronization and resonance between vorticity  
702 waves in shear flow instability. *Physical Review E* **100** (4), 043105.
- 703 HOLLEMAN, R.C., GEYER, W.R. & RALSTON, D.K. 2016 Stratified turbulence and mixing efficiency in a salt  
704 wedge estuary. *J. Phys. Oceanogr.* **46**, 1769–1783.
- 705 HOWARD, L.N. 1961 Note on a paper of John W. Miles. *J. Fluid Mech.* **10**, 509–512.

- 706 KAMINSKI, ALEXIS K, D'ASARO, ERIC A, SHCHERBINA, ANDREY Y & HARCOURT, RAMSEY R 2021 High-  
707 resolution observations of the north pacific transition layer from a lagrangian float. *Journal of*  
708 *Physical Oceanography* **51** (10), 3163–3181.
- 709 KAMINSKI, A. K. & SMYTH, W. D. 2019 Stratified shear instability in a field of pre-existing turbulence. *J.*  
710 *Fluid Mech.* **863**, 639–658.
- 711 KLAASSEN, G.P. & PELTIER, W.R. 1985 The onset of turbulence in finite-amplitude Kelvin-Helmholtz billows.  
712 *J. Fluid Mech.* **155**, 1–35.
- 713 KLAASSEN, G.P. & PELTIER, W.R. 1989 The role of transverse secondary instabilities in the evolution of free  
714 shear layers. *J. Fluid Mech.* **202**, 367–402.
- 715 KLAASSEN, G.P. & PELTIER, W.R. 1991 The influence of stratification on secondary instability in free shear  
716 layers. *J. Fluid Mech.* **227**, 71–106.
- 717 LASHERAS, JC & CHOI, H 1988 Three-dimensional instability of a plane free shear layer: an experimental  
718 study of the formation and evolution of streamwise vortices. *Journal of Fluid Mechanics* **189**, 53–86.
- 719 LEE, V. & CAULFIELD, C.P. 2001 Nonlinear evolution of a layered stratified shear flow. *Dyn. Atmos. Oc.* **34**,  
720 103–124.
- 721 LEWIN, S. F. & CAULFIELD, C. P. 2021 The influence of far-field stratification on turbulent mixing. *J. Fluid*  
722 *Mech.* **928**, A20.
- 723 LIAN, Q., SMYTH, W. D. & LIU, Z. 2020 Numerical computation of instabilities and internal waves from  
724 in situ measurements via the viscous Taylor-Goldstein problem. *J. Atmos. Oceanic Technol.* **37** (5),  
725 759–776.
- 726 LIU, CHIH-LUN, KAMINSKI, ALEXIS K & SMYTH, WILLIAM D 2022 The butterfly effect and the transition to  
727 turbulence in a stratified shear layer. *Journal of Fluid Mechanics* **953**, A43.
- 728 LIU, CHIH-LUN, KAMINSKI, ALEXIS K & SMYTH, WILLIAM D 2023 The effects of boundary proximity on  
729 kelvin-helmholtz instability and turbulence. *Journal of Fluid Mechanics* **966**, A2.
- 730 MASHAYEK, A., CAULFIELD, C. P. & PELTIER, W. R. 2013 Time-dependent, non-monotonic mixing in  
731 stratified turbulent shear flows: implications for oceanographic estimates of buoyancy flux. *J. Fluid*  
732 *Mech.* **736**, 570–593.
- 733 MASHAYEK, A. & PELTIER, W. R. 2012a The ‘zoo’ of secondary instabilities precursory to stratified shear  
734 flow transition. Part 1 shear aligned convection, pairing, and braid instabilities. *J. Fluid Mech.* **708**,  
735 5–44.
- 736 MASHAYEK, A. & PELTIER, W. R. 2012b The ‘zoo’ of secondary instabilities precursory to stratified shear  
737 flow transition. Part 2 the influence of stratification. *J. Fluid Mech.* **708**, 45–70.
- 738 MASHAYEK, A. & PELTIER, W. R. 2013 Shear-induced mixing in geophysical flows: does the route to  
739 turbulence matter to its efficiency? *J. Fluid Mech.* **725**, 216–261.
- 740 MILES, J.W. 1961 On the stability of heterogeneous shear flows. *J. Fluid Mech.* **10**, 496–508.
- 741 MOUM, J. N., NASH, J. D. & SMYTH, W. D. 2011 Narrowband, high-frequency oscillations in the upper  
742 equatorial ocean: Part 1: Interpretation as shear instabilities. *J. Phys. Oceanogr.* **41**, 397–411.
- 743 NEWSOM, R.K. & BANTA, R.M. 2003 Shear flow instability in the stable nocturnal boundary layer as observed  
744 by Doppler lidar during CASES-99. *J. Atmos. Sci.* **60**, 16–33.
- 745 OLSTHOORN, JASON, KAMINSKI, ALEXIS K & ROBB, DANIEL M 2023 Dynamics of asymmetric stratified  
746 shear instabilities. *Physical Review Fluids* **8** (2), 024501.
- 747 OSBORN, THOMAS R. 1980 Estimates of the local rate of vertical diffusion from dissipation measurements.  
748 *J. Phys. Oceanogr.* **10**, 83–89.
- 749 PELTIER, W.R. & CAULFIELD, C.P. 2003 Mixing efficiency in stratified shear flows. *Annu. Rev. Fluid Mech.*  
750 **35**, 136–167.
- 751 PETROPOULOS, NICOLAOS, MASHAYEK, ALI & CAULFIELD, COLM-CILLE P. 2023 Turbulent disruption of  
752 density staircases in stratified shear flows. *J. Fluid Mech.* **961**, A30.
- 753 SALEHIPOUR, H. & PELTIER, W.R. 2015 Diapycnal diffusivity, turbulent Prandtl number and mixing efficiency  
754 in Boussinesq stratified turbulence. *J. Fluid Mech.* **775**, 464–500.
- 755 SMYTH, W.D., MAYOR, S.D. & LIAN, Q. 2023 The role of ambient turbulence in canopy wave generation by  
756 Kelvin-Helmholtz instability. *Boundary Layer Met.* <https://doi.org/10.1007/s10546-022-00765-y>.
- 757 SMYTH, W. D. 2003 Secondary Kelvin-Helmholtz instability in a weakly stratified shear flow. *J. Fluid Mech.*  
758 **497**, 67–98.
- 759 SMYTH, W. D. 2006 Secondary circulations in Holmboe waves. *Phys. Fluids* **18**, 06414.
- 760 SMYTH, W. D. 2020 Marginal instability and the efficiency of ocean mixing. *J. Phys. Oceanogr.* **50** (8),  
761 2141–2150.

- 762 SMYTH, W. D. & CARPENTER, J.R. 2019 *Instability in Geophysical Flows*. Cambridge, UK: Cambridge  
763 University Press.
- 764 SMYTH, W. D. & MOUM, J.N. 2001 3d turbulence. In *Encyclopedia of Ocean Sciences* (ed. S. Thorpe J,  
765 Steele & K. Turekian). Academic Press.
- 766 SMYTH, W. D. & MOUM, J. N. 2000 Length scales of turbulence in stably stratified mixing layers. *Phys.*  
767 *Fluids* **12**, 1327–1342.
- 768 SMYTH, W. D., MOUM, J. N. & CALDWELL, D. R. 2001 The efficiency of mixing in turbulent patches:  
769 inferences from direct simulations and microstructure observations. *J. Phys. Oceanogr.* **31**, 1969–  
770 1992.
- 771 SMYTH, W. D. & PELTIER, W. R. 1989 The transition between Kelvin-Helmholtz and Holmboe instability:  
772 an investigation of the overreflection hypothesis. *J. Atmos. Sci.* **46** (24), 3698–3720.
- 773 SMYTH, W. D. & WINTERS, K. B. 2003 Turbulence and mixing in Holmboe waves. *J. Phys. Oceanogr.* **33**,  
774 694–711.
- 775 STAQUET, C. 1995 Two-dimensional secondary instabilities in a strongly stratified shear layer. *J. Fluid Mech.*  
776 **296**, 73–126.
- 777 TAYLOR, JOHN R 2008 *Numerical simulations of the stratified oceanic bottom boundary layer*. University of  
778 California, San Diego.
- 779 TAYLOR, J. R. & ZHOU, Q. 2017 A multi-parameter criterion of layer formation in a stratified shear flow  
780 using sorted buoyancy coordinates. *J. Fluid Mech.* **823**, R5.
- 781 TIMMERMANS, M.-L., TOOLE, J., KRISHFIELD, R. & WINSOR, P. 2008 Ice-tethered profiler observations of  
782 the double-diffusive staircase in the Canada Basin thermocline. *J. Geophys. Res.* **113**, C00A02.
- 783 TSENG, YU-HENG & FERZIGER, JOEL H 2001 Mixing and available potential energy in stratified flows. *Physics*  
784 *of Fluids* **13** (5), 1281–1293.
- 785 TU, JUNBIAO, FAN, DAIDU, LIU, ZHIYU & SMYTH, WILLIAM 2022 Scaling the mixing efficiency of sediment-  
786 stratified turbulence. *Geophysical Research Letters* **49** (13), e2022GL099025.
- 787 VAN HAREN, H., GOSTIAUX, L., MOROZOV, E. & TARAKANOV, R. 2014 Extremely long Kelvin-Helmholtz  
788 billow trains in the Romanche Fracture Zone. *Geophys. Res. Lett.* **41**, 8445–8451.
- 789 WINTERS, K., LOMBARD, P.N., RILEY, J.J. & D'ASARO, E. A. 1995 Available potential energy and mixing in  
790 density-stratified fluids. *J. Fluid Mech.* **289**, 115–128.
- 791 WOODS, J.D. 1968 Wave-induced shear instability in the summer thermocline. *J. Fluid Mech.* **32**, 791–800.